Monthly Notices
of the
ROYAL ASTRONOMICAL SOCIETY

MNRAS **504,** 857–870 (2021)
Advance Access publication 2021 March 27

doi:10.1093/mnras/stab898

Quasars at intermediate redshift are not special; but they are often satellites

Shadab Alam [1]★ Nicholas P. Ross [1] Sarah Eftekharzadeh,[2] John A. Peacock [1] Johan Comparat,[3] Adam D. Myers[4] and Ashley J. Ross [5]

[1]*Institute for Astronomy, University of Edinburgh, Royal Observatory, Blackford Hill, Edinburgh EH9 3HJ, UK*
[2]*Department of Physics and Astronomy, University of Utah, 115 S 1400 E, Salt Lake City, UT 84112, USA*
[3]*Max-Planck-Institut für extraterrestrische Physik (MPE), Giessenbachstrasse 1, D-85748 Garching bei München, Germany*
[4]*Department of Physics and Astronomy, University of Wyoming, Laramie, WY 82071, USA*
[5]*Center for Cosmology and Astro-Particle Physics, Ohio State University, Columbus, 43210 Ohio, USA*

Accepted 2021 March 14. Received 2021 March 13; in original form 2020 July 4

ABSTRACT

Understanding the links between the activity of supermassive black holes (SMBHs) at the centres of galaxies and their host dark matter haloes is a key question in modern astrophysics. The final data release of the SDSS-IV eBOSS provides the largest contemporary spectroscopic sample of galaxies and quasi-stellar objects (QSOs). Using this sample and covering the redshift interval $z = 0.7$–1.1, we have measured the clustering properties of the eBOSS QSOs, emission-line galaxies (ELGs), and luminous red galaxies (LRGs). We have also measured the fraction of QSOs as a function of the overdensity defined by the galaxy population. Using these measurements, we investigate how QSOs populate and sample the galaxy population, and how the host dark-matter haloes of QSOs sample the underlying halo distribution. We find that the probability of a galaxy hosting a QSO is independent of the host dark matter halo mass of the galaxy. We also find that about 60 per cent of eBOSS QSOs are hosted by LRGs and about 20–40 per cent of QSOs are hosted by satellite galaxies. We find a slight preference for QSOs to populate satellite galaxies over central galaxies. This is connected to the host halo mass distribution of different types of galaxies. Based on our analysis, QSOs should be hosted by a very broad distribution of haloes, and their occurrence should be modulated only by the efficiency of galaxy formation processes.

Key words: accretion, accretion discs – black hole physics – galaxies: luminosity function, mass function – quasars: supermassive black holes – large-scale structure of Universe.

1 INTRODUCTION

Two outstanding questions in extragalactic astrophysics are the manner in which galaxies sample the dark matter (DM) halo mass function, and how active galactic nuclei (AGNs) sample the galaxy population. These questions are central because it is now believed that the energy and kinematics associated with AGNs are crucial in understanding how galaxies form and regulate their star formation (see reviews by e.g. Fabian 2012; Kormendy & Ho 2013; Madau & Dickinson 2014; King & Pounds 2015; Somerville & Davé 2015; Padovani et al. 2017; Xue 2017).

Although they are rare, quasi-stellar objects (QSOs) (generally defined as luminous AGNs with bolometric luminosities $L_{\rm bol}$ above $\sim 10^{38}$ W) have become key tracers of the large-scale structure (LSS) of the Universe (e.g. Coil et al. 2004; Outram et al. 2004; Croom et al. 2005; Myers et al. 2007; Shen et al. 2007; da Ângela et al. 2008; Ross et al. 2009; He et al. 2018; Hou et al. 2021; Neveux et al. 2020; Oogi et al. 2020). However, the detailed link between central black holes and their DM haloes is still poorly understood.

In the case of a Gaussian random field, the two-point correlation function (2PCF) statistic provides a full characterization of LSS (see e.g. Peebles 1980; Bardeen et al. 1986; Wang et al. 2013). A given LSS tracer will display biased clustering, with an amplitude that increases for objects associated with rare massive haloes. Thus, by measuring the 2PCF of QSOs and assuming an underlying form of the DM halo mass function, it is possible to associate the QSOs with a given DM halo mass. The bias parameter, b, is typically determined on linear scales ~ 5–$30\,h^{-1}$Mpc, and this measurement and comparison has been carried out for a range of QSO redshifts, luminosities, and colours.

Results from the last 10–20 yr have traditionally placed QSOs in a mean DM halo mass of a few $\times\ 10^{12}{\rm M}_{\odot}$ (e.g. Croom et al. 2005; Coil et al. 2007; Myers et al. 2007; da Ângela et al. 2008; Ross et al. 2009). However, one critical drawback of these measurements is that often only a single 'typical' halo mass is reported; given the very large range of black hole masses in QSOs ($M_{\rm BH} = 10^{6}$–$10^{10}\,h^{-1}{\rm M}_{\odot}$), this single effective halo mass is relatively uninformative. Ideally, one would like to understand the full distribution of halo masses associated with QSOs, and then relate this to the underlying DM halo mass functions, and indeed to the way in which galaxies in general populate haloes. Are QSOs a subset of the full galaxy population? Or is luminous

★ E-mail: shadab.zamman@gmail.com

AGN activity found preferentially in one type of galaxy? Or in a particular environment?

An exception to the 'single halo mass' approach is White et al. (2012) who assume that QSOs reside in haloes with a lognormal distribution of masses, centred on a characteristic mass that scales with luminosity. This model results in masses for luminous QSOs at redshift $z \approx 2.4$ in the range $0.8–4 \times 10^{12}\,h^{-1}\mathrm{M}_{\odot}$, with a central value of $2 \times 10^{12}\,h^{-1}\mathrm{M}_{\odot}$. Miyaji et al. (2011) and Krumpe et al. (2012) also studied the cross-correlation of *ROSAT* AGNs with SDSS galaxies and constrain the host halo mass distribution of the *ROSAT* AGNs. They predict that the satellite fraction of AGNs reduces with host halo mass in contrast to luminous galaxies.

Several groups and authors have used the 2PCF to infer the halo occupation distribution (HOD) of the QSO population, and the 'satellite fraction'. The HOD provides a complete description of the relation between QSOs and DM at the level of individual virialized haloes (Berlind & Weinberg 2002; Kravtsov et al. 2004; Zheng et al. 2005; Chatterjee et al. 2012; Richardson et al. 2012). The QSO HOD is defined by $P(N|M_h)$, the conditional probability that a halo of virial mass M_h contains N QSOs above some specified (luminosity) threshold. A DM halo may contain zero, one, or more than one QSO. If more than one, the most massive galaxy is deemed to be at the centre of the potential well, and the less massive QSO(s) are the 'satellites' in that halo (even though they may still be relatively massive, e.g. $\gtrsim 10^{11}\mathrm{M}_{\odot}$ themselves).

Richardson et al. (2012) present estimates of the 2PCF for QSOs, and interpret them with the HOD framework. In order to explain the small-scale clustering, the HOD model requires that a small fraction, $f_{\rm sat} = (7.4 \pm 1.4) \times 10^{-4}$, of the QSOs be satellites in DM haloes at $z \simeq 1.4$. The median masses of the host haloes of central and satellite QSOs at these redshifts are constrained to be $M_{\rm cen} = 4.1^{+0.3}_{-0.4} \times 10^{12}\,h^{-1}\mathrm{M}_{\odot}$ and $M_{\rm sat} = 3.6^{+0.8}_{-1.0} \times 10^{14}\,h^{-1}\mathrm{M}_{\odot}$, respectively. Note that even though centrals are expected to be the most massive QSOs in a given halo the satellites resides only in the massive haloes, whereas centrals QSOs can be found in relatively low-mass haloes. Therefore, the median mass of host haloes of satellites QSOs is found to be two order of magnitude larger than central QSOs.

Shen et al. (2013) also present measurements of the 2PCF, this time via the cross-correlation of $\simeq$8200 SDSS QSOs and $\simeq$350 000 massive red galaxies from the SDSS-III Baryonic Oscillation Spectroscopic Survey (BOSS) at $0.3 < z < 0.9$. They estimate a QSO linear bias of $b_{\rm Q} = 1.38 \pm 0.10$ at $\langle z \rangle = 0.53$ corresponding to a characteristic host halo mass of $4 \times 10^{12}\,h^{-1}\mathrm{M}_{\odot}$ (compared with a characteristic host halo mass for galaxies of $10^{13}\,h^{-1}\mathrm{M}_{\odot}$). Comparing these measurements with HOD models suggests that QSOs reside in a broad range of host haloes. The host halo mass distributions significantly overlap with each other for QSOs at different luminosities, implying a poor correlation between halo mass and instantaneous QSO luminosity. Shen et al. (2013) also find that the QSO HOD parametrization is largely degenerate such that different HODs can reproduce the cross-correlations equally well, but with different satellite fractions and host halo mass distributions.

Georgakakis et al. (2019) study the distribution of AGN host haloes using semi-empirical modelling. This model was shown to be consistent with current clustering measurements and found that AGNs host halo mass distribution is broad. They also predict that the fraction of satellite AGNs increases towards the massive haloes.

The Sloan Digital Sky Survey (SDSS) has been the state-of-the-art in spectroscopic QSO surveys for the last 15 yr. The Extended Baryon Oscillation Spectroscopic Survey (eBOSS) is the culmination of the SDSS-I, -II, -III, and -IV quasar programmes and has recently completed a spectroscopic survey of >500 000 QSOs over 6000 square degrees, covering redshifts $0.7 < z < 3.5$ (Lyke et al. 2020). eBOSS is currently the premier data set to measure QSO clustering (Ross et al. 2020). In near future eROSITA (Merloni et al. 2012) will provide the most promising X-ray AGN sample.

Eftekharzadeh, Myers & Kourkchi (2019) measure the quasar clustering signal across four orders of magnitude in scale, ($0.01 \lesssim r_p \lesssim 100\,h^{-1}$Mpc) at $z \simeq 1.5$ using data from eBOSS. Using the HOD prescription, these authors find a satellite fraction of $f_{\rm sat} = 0.071^{+0.009}_{-0.004}$ and minimum mass of $M_{\rm min} = 2.31^{+0.41}_{-0.38} \times 10^{12}\,h^{-1}\mathrm{M}_{\odot}$ for the host DM haloes best describes the quasar clustering on all scales. Rodríguez-Torres et al. (2017) used a modified Sub-halo abundance matching method to model eBOSS QSOs showing the mean host halo mass of $5 \times 10^{12}\,h^{-1}\mathrm{M}_{\odot}$.

In this paper, we extend these measurements of the clustering of galaxies and QSOs in eBOSS in order to: (i) understand the relation of the active QSOs to the general galaxy population; and (ii) understand the relation of the LSS traced by the QSOs to the underlying DM halo distribution.

We will make progress by employing and expanding on recent work using the 'Multi-Tracer HOD' model (MTHOD: Alam et al. 2020, hereafter Paper I) and apply this method to the latest version (Data Release 16) of the SDSS-IV eBOSS data. Our goal is to investigate a series of HOD models that described how QSOs populate the distribution of DM haloes. We will use the luminous red galaxies (LRGs) and the emission-line galaxies (ELGs) that inhabit the same cosmological volume as the QSOs to perform these tests and investigations. This will allow us to discriminate between the models.

This paper is organized as follows. In Section 2, we present our data sample. In Section 3, we describe the techniques involved in our measuring the 2PCF, and note several effects that could give rise to systematics in the measurements. In Section 4, we describe our MTHOD model and our Galaxy-QSO Occupation Distribution (GQOD) model that we use to model the galaxy and AGN population. In Section 5, we present our clustering measurements and the derived parameters. In Section 6, we place our new results in a broad context and note our main findings. We conclude in Section 7. Appendix A gives technical details. We assume a flat Λ cold dark matter (ΛCDM) cosmology with $\Omega_{\rm m} = 0.307$, $\Omega_b = 0.048$, $h = 0.67$, $n_s = 0.96$, and $\sigma_8 = 0.82$. Our assumed cosmology is close to the best-fitting parameters reported in Planck Collaboration (2020) and motivated by the fiducial cosmology assumed in the N-body simulation (MultiDark Planck simulation, MPDL2; Prada et al. 2012) that we employ in our HOD models.

2 DATA

In this section, we describe the spectroscopic data from the SDSS eBOSS survey that we will use for our clustering measurements. We also will utilize new deep public imaging data from the Hyper Suprime-Cam (HSC) Subaru Strategic Programme.

2.1 SDSS-IV: eBOSS

We use data obtained from the extended Baryon Oscillation Spectroscopic Survey (eBOSS: Dawson et al. 2013). This is one of the programmes of the wider 5 yr Sloan Digital Sky Survey-IV (SDSS-IV; Blanton et al. 2017) using the BOSS spectrograph (Smee et al. 2013) on the Sloan Telescope (Gunn et al. 2006).

The primary science goal of eBOSS was to measure the expansion of the Universe via LSS spectroscopic surveys. To achieve this,

Table 1. The number of objects from each selection used in this study. The approximate number density, in units of $10^{-5}(h^{-1}\,\mathrm{Mpc})^{-3}$, is also given.

Sample	Number of objects	$n(z = 0.86)$	Overlap area with QSOs (deg^2)
ELG	185 789	40	674
LRG	98 086	10	4237
QSOs	57 484	2	4808

eBOSS comprises four different tracers: LRGs (with a redshift range $0.6 < z < 1.0$), ELGs ($0.6 < z < 1.1$), QSOs ($0.7 < z < 3.5$), and Lyman-α forest traced by QSOs ($z > 2.1$).

We use a subset of the eBOSS samples covering two fields between redshifts 0.7 and 1.1 where LRGs, ELGs, and QSOs overlap in volume. The QSOs and LRGs sample the same area of the sky, but the ELG sky coverage is smaller. However, the ELG volume lies mostly inside the QSO/LRG volume by construction. Using the cross-correlation clustering technique, this overlap region can be also used to study the environmental dependence of QSOs, resulting in a sampling of the underlying DM distribution. We now briefly describe the relevant aspects of eBOSS sample selection, with more details being given by Prakash et al. (2016) for LRGs, Raichoor et al. (2017) for ELGs, and Myers et al. (2015) for QSOs. Table 1 gives the number of objects from each selection used in this study. The total volume where all three tracers are observed is 0.64 h^{-3} Gpc^3 between redshifts of 0.7 and 1.1.

2.2 LRG selection

The LRGs are the most luminous and reddest galaxies, residing in massive DM haloes with high bias. The eBOSS LRGs are selected from SDSS imaging data (Albareti et al. 2017) in combination with infrared photometry from WISE (Wright et al. 2010) using the following target selection rules:

$$r - i > 0.98 \tag{1}$$

$$r - W1 > 2(r - i) \tag{2}$$

$$i - z > 0.625, \tag{3}$$

where r, i, and z are the 'model' magnitudes of the SDSS photometric bands and W1 refers to the WISE magnitude in the 3.4 μm channel. The selections in equations (1), (2), and (3) are designed to achieve the redshift range, reduce stellar contamination, and reduce low-z interlopers, respectively. The details of how these rules were derived and additional considerations are discussed in Prakash et al. (2016).

2.3 ELG selection

The eBOSS ELGs are expected to be star-forming galaxies at high redshift, and are thus selected based on high O II flux. The ELG sample is selected from DECAM Legacy survey (DECaLS: Dey et al. 2019). The target selection of ELGs in the North Galactic Cap (NGC) and South Galactic Cap (SGC) is slightly different due to availability of deeper data in SGC. We only use the SGC part of the ELG sample due to overlap with other tracers hence we only describe the SGC selection here. The ELG selection has two parts; the first part is to select star-forming galaxies corresponding to O II emission lines using the g band flux cuts

$$21.825 < g < 22.825. \tag{4}$$

The second rule for ELG selection is to preferentially select galaxies around redshift 1.0 given by following equations:

$$-0.068(r - z) + 0.457 < g - r < 0.112(r - z) + 0.773 \tag{5}$$

$$0.218(g - r) + 0.571 < r - z < -0.555(g - r) + 1.901, \tag{6}$$

where g, r, and z are the observed magnitude in DECaLS g, r, and z photometric bands. More details of how these rules were derived and additional considerations are discussed in Raichoor et al. (2017).

2.4 Quasar (QSO) selection

Myers et al. (2015) describe in detail the requirements and how the eBOSS QSO sample is selected. First a supersample of QSOs is selected from SDSS imaging with either $g < 22$ or $r < 22$ and $i_f > 17$, where g and r are the PSF magnitude of SDSS photometric bands and i_f is the FIBER2MAG. This supersample is passed through the XDQSOz algorithm (Bovy et al. 2012), which assigns a probability for each object of being a QSO in a given redshift range. The eBOSS sample uses a probabilistic cut of $P_{\mathrm{QSO}}(z > 0.9) > 0.2$. An infrared cut in WISE imaging is also used to remove stellar contamination. The final QSOs sample with good redshifts is obtained using (IMATCH=1 or 2) along with a target completeness cut ($C_{\mathrm{eBOSS}} > 0.5$) and spectroscopic completeness cut ($C_z > 0.5$) as described in Ross et al. (2020).

2.5 Quasar brightest 50 per cent sample

We would also like to investigate how quasars populate their DM haloes as a function of QSO luminosity. QSO luminosity should depend on supermassive black hole (SMBH) mass and mass accretion rate. With the link between SMBH mass and bulge mass established at low ($z \lesssim 0.1$) redshift, and with a connection between bulge and halo mass, one might suspect that more luminous quasars (with more massive SMBHs) might populate their DM haloes in a different manner.

We split the full QSO sample into the brightest 50 per cent of objects, as given by their i-band absolute PSF magnitude, noting that the observed i-band samples 3660–4530Å rest-frame wavelength at $z = 0.86$, where there are no strong broad emission lines. This is 28 742 objects which we call this sample the 'Brightest 50 per cent'.

The top panel of Fig. 1 shows a $\sim 4 \times 2\,\mathrm{deg}^2$ patch of eBOSS between redshifts 0.82 and 0.88. The three tracers LRG, ELG, and QSO are shown in red, blue, and cyan coloured filled symbols, respectively. The size of the symbols represents the absolute r-band (AB) magnitude of individual objects. This clearly shows that QSOs are rare and bright compared to the LRGs and ELGs. The bottom panel of Fig. 1 shows the number density distribution of each tracer in our sample. In this paper, we apply redshift cuts at $z = 0.7$ and $z = 1.1$ for our analysis. We note that around redshift $z = 0.86$, the mean redshift of our measurements, the number density of LRG, ELG, and QSO are 10^{-4}, 4×10^{-4}, and 2×10^{-5} $\left[h^{-1}\mathrm{Mpc}\right]^{-3}$, respectively. The redshift distribution of the Brightest 50 per cent QSO sample is also shown in the bottom panel. The redshift distribution of the full QSO and Brightest 50 per cent QSO samples are the same, so a direct comparison between the two is reasonable.

2.6 HSC imaging

Deep imaging data from HSC (Miyazaki et al. 2018) exist for a portion of our spectroscopic data. Imaging data from the the Hyper

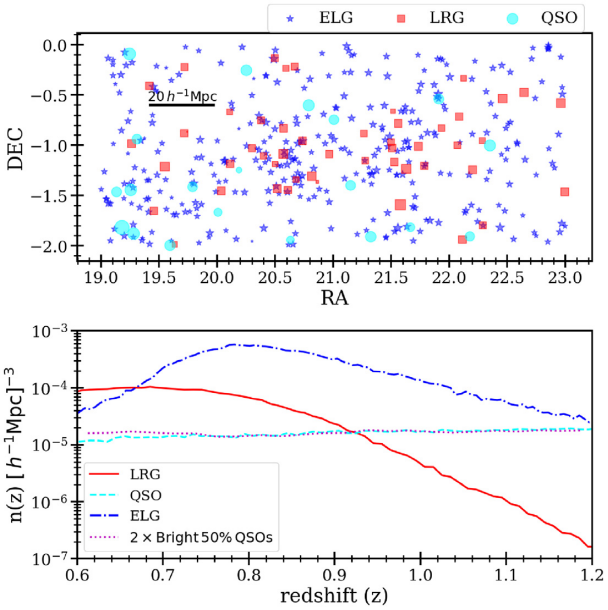

Figure 1. Sky coverage and number density distribution of our sample used in this paper. The top panel shows a $\sim 4 \times 2\,\mathrm{deg}^2$ patch of the eBOSS sample between redshifts 0.82 and 0.88. The three tracers LRG, ELG, and QSO are shown in red squares, blue stars, and cyan circles, respectively. The varying symbol sizes represent the absolute AB r-magnitude of each individual object. This clearly shows that QSOs are rare and bright compared to LRG and ELG galaxies. The bottom panel shows the number density distribution of each tracer in our sample. The red solid line, blue dot–dashed line, and cyan dashed line represent LRG, ELG, and QSO, respectively. In this paper, we apply a redshift cut at 0.7 and 1.1 for our analysis.

Suprime-Cam Subaru Strategic Programme (HSC-SPP) cover part of the sky shown in Fig. 1. Using the 8.2m Subaru Telescope (Iye et al. 2004), the HSC-SSP (Aihara et al. 2018, 2019) currently offers the best combination of depth and image quality for a ground-based survey. The Wide Layer achieves depths of $g = 26.6$, $r = 26.2$, $i = 26.2$, $y = 25.3$, and $z = 24.5$ in the five broad-band filters. The seeing ranges from 0.58 to 0.77 arcsec (Aihara et al. 2019). All data products are available for the Second Data Release at https://hsc-release.mtk.nao.ac.jp/doc/.

The HSC-SSP data are of high enough quality to see galaxy groups out to $z \sim 1$ (e.g. Umetsu et al. 2020). Thus, we will use the HSC data to visually inspect the environments of the $z = 0.7$–1 eBOSS QSOs.

3 MEASUREMENTS AND SYSTEMATICS

3.1 Clustering and the 2PCF

Here, we give a brief description of the 2PCF; for a more formal treatment the reader is referred to e.g. Peebles (1980). The 2PCF, $\xi(r)$, is defined by the joint probability that two objects (e.g. galaxies) are found in the two volume elements $\mathrm{d}V_1$ and $\mathrm{d}V_2$ placed at separation r,

$$\mathrm{d}P_{12} = n^2[1 + \xi(r)]\mathrm{d}V_1\mathrm{d}V_2, \tag{7}$$

with n being the object number density. To calculate $\xi(r)$, N points are given inside a window W of observation, which is a 3D body of volume $V(W)$. We calculate the position of each galaxy in three-dimensional space by converting the measured redshift to a line-of-sight distance using our fiducial cosmology. As usual, we also generate a catalogue of random points, with the same window function W as the data, but without correlated positional information.

We then measure the galaxy autocorrelation function using the minimum variance Landay–Szalay estimator (Landy & Szalay 1993) given by

$$\xi_{\mathrm{auto}}(\vec{r}) = \frac{DD(\vec{r}) - 2DR(\vec{r}) + RR(\vec{r})}{RR(\vec{r})}, \tag{8}$$

where DD, DR, and RR are the number of galaxy–galaxy, galaxy–random, and random–random pairs as a function of vector separation in three-dimensional space. The galaxy, QSO, and random catalogues for the LSS measurements for the SDSS DR16 sample are publicly available.[1]The cross-correlations are measured using the following estimator:

$$\xi_{\mathrm{cross}}(\vec{r}) = \frac{D_1D_2(\vec{r})}{D_1R_2(\vec{r})} - 1, \tag{9}$$

where D_1D_2 and D_1R_2 are the number of galaxy–galaxy and galaxy–random pairs from different samples. As is conventional, we project the three-dimensional space on to a two-dimensional space that decomposes pair separation vectors along the line of sight ($r_{\shortparallel}$) and perpendicular to the line of sight ($r_\perp$, or r_p). This gives us the two-dimensional correlation function $\xi(r_p, r_{\shortparallel})$,

$$w_p(r_p) = \int_{r_1}^{r_2} \xi(r_p, r_\parallel)\,\mathrm{d}r_\parallel. \tag{10}$$

In practice, we measure the projected correlation (w_p) by integrating the two-dimensional correlation function along the line of sight between $r_\parallel = -40\,h^{-1}$Mpc and $r_\parallel = +40\,h^{-1}$Mpc and using 25 equally spaced bins in logarithmic scale for $r_\perp$ between 0.1 and $30\,h^{-1}$Mpc. Typically, the projected correlation function is integrated to $r_\parallel = 100\,h^{-1}$Mpc or larger to avoid the need to model redshift space clustering. But our model is evaluated in redshift space with full non-linearity and hence we do not have any constraint on minimum $r_{\shortparallel}$ for the projected correlation function. The projected correlation function $w_p(r_p)$ helps us constrain the HOD parameters that govern the galaxy-halo connection. To estimate the errors of our measurements, we create 86 jackknife regions for our sample and calculate the jackknife covariance of the w_p measurements. Note that our jackknife region in the overlap sky area corresponds to approximately 6 deg $\times$ 1.3 deg. The 1.3 deg at the mean redshift of the sample corresponds to roughly $40\,h^{-1}$Mpc and hence large enough for our measurements.

3.2 Potential systematic errors

The clustering measurement is sensitive to the completeness of the observed galaxy sample for a given selection scheme. Therefore, it is important to account for variation in the number of detected galaxies as a function of their position in the sky, plus various selection biases due to the systematic errors introduced by instrumentation and measurement.

The number of detected galaxies and the spectroscopic success rate can be correlated with, for example, stellar density, extinction, sky brightness, airmass, or position in the fibre plate (see e.g. Bolton et al. 2012). To remove these correlations, Ross et al. (2012) introduced the use of systematic weights, and the use of systematic weights for LRGs, QSOs, and ELGs is investigated by Bautista et al. (2018), Gil-Marín et al. (2018), and Raichoor et al. (2021), respectively. We

[1]https://data.sdss.org/sas/dr16/eboss/

show in Paper I that measurement of w_p at scales in the range $\simeq$ 1–30 h^{-1}Mpc is insensitive to the resulting corrections by any of the introduced systematic weights. We also note that due to fibre collision the galaxy sample becomes highly incomplete below the fibre scale, which is approximately 65 arcsec on the sky, corresponding to a scale of $\simeq 0.5h^{-1}$ Mpc at $z = 0.86$ (Anderson et al. 2012; Guo, Zehavi & Zheng 2012; Bianchi & Percival 2017). For the purpose of this paper we will not use the measurements or our models at scales smaller than the fibre collisions.

3.3 Environmental measures

We also measure galaxy environment following the method described in Alam et al. (2019). Here, we briefly summarize the method. We focus on the measurement of local overdensity of galaxies around our sample.

In order to measure galaxy overdensity, we first create the Voronoi tessellation of the survey volume using the method developed in Alam et al. (2019). This partitions the volume into disjoint cells each containing only one galaxy. We use the random catalogue provided with the Large Scale Structure catalogue and count the number of randoms in each Voronoi cell ($N_{\rm cell}^{\rm rand}$). We then estimate the density as the ratio of the mean density of randoms ($n_{\rm rand}$) to the random counts for each cell, and associate this with the galaxy in that cell, $\rho_{\rm cell}$:

$$\rho_{\rm cell} = \frac{n_{\rm rand}}{N_{\rm cell}^{\rm rand}}. \tag{11}$$

The measured density is then smoothed at this chosen scale to determine the smoothed density ($\rho_{\rm smth}$) as

$$\rho_{\rm smth}(\vec{r}_0) = \int \rho_{\rm cell}(\vec{r})\mathcal{N}(\vec{r} - \vec{r}_0, \sigma_{\rm smth})\,{\rm d}^3 r \tag{12}$$

with $\sigma_{\rm smth} = 5\,h^{-1}$Mpc. This is then converted to an overdensity, δ_5:

$$\delta_5 = \frac{\rho_{\rm smth}}{\bar{\rho}_{\rm smth}} - 1. \tag{13}$$

This allows us to assign a value of δ_5 for each QSO and galaxy in the observed sample living in the overlapped volume. We finally measure QSO fraction as the function of δ_5 using

$$f_{\rm QSO}(\delta) = \frac{C_{\rm QSO}(\delta;\Delta)}{C_{\rm LRG}(\delta;\Delta) + C_{\rm ELG}(\delta;\Delta) + C_{\rm QSO}(\delta;\Delta)}, \tag{14}$$

where $\delta = \log_{10}(1 + \delta_5)$ and $C_{\rm tracer}(\delta;\Delta)$ gives the weighted count of number of object of a particular tracer with δ between $\delta - \Delta$ and $\delta + \Delta$. In these counts, we only consider objects with $-1 < \delta < 1$ and divide this in five bins with $\Delta = 0.1$. We use only five bins in order to keep the size of the covariance matrix small while still having the overall trend of $f_{\rm QSO}$ with δ. Each object in the sample is weighted such that the redshift distributions of all objects are the same.

4 MODELLING THE GALAXY AND QSO POPULATIONS

Our aim is to use the (cross-)clustering measurements of the LRG, ELG, and QSO populations as constraints for our HOD models in order to understand the QSO population.

We employ two HOD models: (i) the MTHOD model to model the overall galaxy population and (ii) the GQOD model in order to model the statistical properties of QSOs as a distinct subpopulation from the parent galaxy population. The *anzatz* we use to model the QSO population is that the AGNs observed as QSOs are *not special* in their inherent host galaxy properties, but are a subsample of the global galaxy population.

4.1 MTHOD galaxy catalogues

To model the galaxy population we use the MTHOD model and catalogue of Paper I. The MTHOD model introduces a new approach to model multiple tracers in the same volume. In general each of the tracers can have its own occupation recipe for the central and satellite galaxies. At the same time, the MTHOD ensures that the joint occupation probabilities are well behaved by limiting the total probability of central galaxies in a halo to 1. It also forbids the non-physical situation of multiple types of galaxies at the centre of the same DM halo. The key parameters in MTHOD models are the separate parameters for the occupation probability of central and satellite galaxies for each tracer; these are given in the Appendix.

The MTHOD mock galaxy catalogue is created using the MPDL2 (Prada et al. 2012) publicly available through the CosmoSim data base.[2] MPDL2 is a DM-only N-body simulation using the GADGET-2 algorithm (Klypin et al. 2016). MDPL2 assumes a flat ΛCDM cosmology with $\Omega_{\rm m} = 0.307$, $\Omega_b = 0.048$, $h = 0.67$, $n_s = 0.96$, and $\sigma_8 = 0.82$, and is a periodic box of side length $1000\,h^{-1}$Mpc sampled by 3840^3 particles. A halo catalogue is generated using the ROCKSTAR[3] halo finder (Behroozi, Wechsler & Wu 2013) at an effective redshift of $z = 0.86$.

The DM haloes are then populated using the following equations for central and satellite galaxies as a function of halo mass, $M_{\rm halo}$:

$$p_{\rm cen}^{\rm tot}(M_{\rm halo};\vec{\theta}) = \sum_{{\rm tr}\,\epsilon\,{\rm TR}} p_{\rm cen}^{\rm tr}(M_{\rm halo};\theta^{\rm tr}) \tag{15}$$

$$\left\langle N_{\rm sat}^{\rm tot}\right\rangle(M_{\rm halo};\vec{\theta}) = \sum_{{\rm tr}\,\epsilon\,{\rm TR}} \left\langle N_{\rm sat}^{\rm tr}\right\rangle(M_{\rm halo};\theta^{\rm tr}), \tag{16}$$

where the sum is over all tracers in the list, TR = {LRG, QSO, ELG}. This equation requires a constraint of $p_{\rm cen}^{\rm tot} \leq 1$ for any halo mass. In paper I, all three tracers (i.e. LRGs, ELGs, and QSOs) are modelled within the MTHOD framework. However, in this paper, we take a different approach. We only use the LRG and ELG galaxies, and do not use the QSOs from the default model. Using the MTHOD mock catalogue, we can measure the clustering and the central/satellite properties for the LRG and ELG populations.

We assume that the MTHOD galaxy catalogue models the complete set of galaxies that host eBOSS QSOs. The MTHOD model samples galaxies starting from a minimum halo mass of $2.1 \times 10^{11}{\rm M}_\odot$. The mean halo mass of eBOSS QSOs is shown to be $5 \times 10^{12}{\rm M}_\odot$ (see fig. 4 of Paper I). The eBOSS galaxies thus cover the entire halo mass range needed to model the eBOSS QSO selection. Therefore, in the absence of any strong environmental effect or assembly bias, it is reasonable to assume that the MTHOD galaxy catalogue models the complete set of galaxies that host eBOSS QSOs. We do expect this assumption to fail in detail (as indicated by fig. 8 of Paper I) but this should be a second-order effect given the current available constraints on such effects.

4.2 GQOD model

A second model, the GQOD model, is employed to model the statistical properties of QSOs as a distinct subpopulation from the

[2] https://www.cosmosim.org/cms/simulations/mdpl2/
[3] https://bitbucket.org/gfcstanford/rockstar

Table 2. Parameters of GQOD models.

Parameters	Description	Used with
$f_{\rm on}(M_{\rm halo})$	This models the probability of a galaxy to turn on with a given host halo mass. This is modelled as a linear spline with 8 knots at locations $\log_{10}(M_{\rm knots}) = [11.2, 11.8, 12.15, 12.5, 12.75, 13.0, 13.5, 15.2]$ It also require the constraint of $\int_0^\infty f_{\rm on}(M_{\rm halo}) n_{\rm gal}(M_{\rm halo}) {\rm d}M_{\rm halo} = n_{\rm QSO}$ where $n_{\rm gal}(M_{\rm halo})$ and $n_{\rm QSO}$ are the number density of galaxies and QSO, respectively.	Inherent and enforced
$G_{\rm type}$	Probability of galaxy to turn into QSO given its host galaxy type $p(G_{\rm type} = {\rm LRG}) = f_{\rm LRG}$ $p(G_{\rm type} = {\rm ELG}) = 1 - f_{\rm LRG} = f_{\rm ELG}$	Inherent and enforced
$G_{\rm pos}$	Probability of galaxy to turn into QSO given its host galaxy position $p(G_{\rm pos} = {\rm satellite}) = f_{\rm sat}$ $p(G_{\rm pos} = {\rm central}) = 1 - f_{\rm sat}$	Only for enforced $f_{\rm sat}$

parent MTHOD galaxy population. The probability of a galaxy being a QSO is given by

$$P_{\rm QSO}(M_{\rm halo}, G_{\rm type}, G_{\rm pos}) = f_{\rm on}(M_{\rm halo}) p(G_{\rm type}) p(G_{\rm pos}), \quad (17)$$

where $f_{\rm on}$ is the probability for the galaxy to turn on with a given host halo mass, $p(G_{\rm type})$ is the probability for a galaxy to be a QSO given its host galaxy type, and $p(G_{\rm pos})$ is the probability for a galaxy to be a QSO given its host galaxy position (central/satellite). A summary of these key parameters of the GQOD model are given in Table 2 and we do consider the three probabilities to be independent of each other. Here, 'turn on' is shorthand for the physical processes involved having sufficient mass accretion in the QSO central engine that the QSO becomes luminous enough to be detected in our survey volume.

We assume $f_{\rm on}$, the fraction of galaxies that will have a QSO turn on, is a function of DM halo mass, $M_{\rm halo}$. This might have a wide distribution in halo mass (see e.g. the deduced wide range of halo mass for central galaxies in Richardson et al. 2012, 2013). Alternatively, QSOs might reside in DM haloes of a certain particular mass range and hence the turn-on probability will have a narrow distribution with halo mass (see e.g. Kayo & Oguri 2012; Eftekharzadeh et al. 2019). We model $f_{\rm on}(M_{\rm halo})$ with a 'linear spline sampling' of eight halo masses between 10^{11} and $10^{15}\, h^{-1}{\rm M}_\odot$.

Moving to $G_{\rm type}$ – the probability that a host galaxy of a QSO may depend on host galaxy type – we introduce the parameter $f_{\rm LRG}$ to define the fraction of QSOs with LRG host galaxies in the sample. We define $f_{\rm LRG} = 1$ to mean that *only* LRGs can host QSOs; consequently, $f_{\rm LRG} = 0$ will mean that only ELGs can be QSO hosts. If the posterior likelihood of either of these extremes is zero, then we can rule out the QSOs being turned on in only one type of galaxy. In a model where the QSO probability is independent of host galaxy type, the fraction of QSOs with a given type of host galaxy should be the same as the fraction of the host galaxy type in the parent population. $f_{\rm LRG}$ (and thus $f_{\rm ELG} = 1 - f_{\rm LRG}$) can be measured directly from data, as is done in Paper I (fig. 7). However, the match between the measured and modelled $f_{\rm LRG}$ and $f_{\rm ELG}$ is very close, so we are able to just use the smoother models.

The probability a host galaxy is a QSO may also depend on 'position', that is, whether it is a central or satellite galaxy. Studies including Zheng et al. (2009) and Richardson et al. (2012, 2013) assumed different halo distributions for central and satellite galaxies, while Kayo & Oguri (2012) and Eftekharzadeh et al. (2019) assumed the halo to be indifferent in hosting a QSO as either a satellite or central galaxy. We include the parameter $G_{\rm pos}$ to encapsulate the positional information.

We adopt two model flavours to study this aspect of QSO physics. In the first flavour, there is no dependence of QSO probability on whether the host galaxy is a central or satellite. Thus, the fraction of QSOs hosted by satellite galaxies will be equal to the fraction of satellite galaxies in the parent population. We call this an 'inherent' satellite fraction and label it '$f_{\rm sat}$ (inherent)'. In the second flavour, the QSO probability can depend on whether the host galaxy is a satellite or a central and this is denoted by an additional parameter, $f_{\rm sat}$. This allows an extra degree of freedom where the satellite fraction in the QSO population does not have to represent the satellite fraction of the parent galaxy population. We call this an 'enforced' satellite fraction, labelled '$f_{\rm sat}$ (enforced)'.

The full list of parameters in our model is given in Table 2. We have a total of nine parameters in the inherent $f_{\rm sat}$ model with eight of them to model the halo mass dependence of $f_{\rm on}$ using linear spline with 8 knots listed in Table 2 and the ninth parameter is to model fraction of QSO with host galaxy as LRG ($f_{\rm LRG}$). The enforced $f_{\rm sat}$ model has an additional 10th parameter to model the fraction of QSOs that are satellite galaxies $f_{\rm sat}$.

Once we have simulated the QSO catalogue, we can predict the projected autocorrelation of quasars as well as the cross-correlation of quasars with LRGs and ELGs. Given the denser galaxy population one can also measure the fraction of QSOs as a function of overdensity. We use these four measurements to constrain the parameters of the model.

4.3 Model constraints and parameter estimation

For any point in the parameter space one can evaluate the probability of a galaxy to turn on using equation (17) and hence obtain a sample of QSOs in the MTHOD catalogue. The LRG-auto, ELG-auto, and LRG×ELG cross-clustering measurements are used to constrain the MTHOD model. Since these are presented in Paper I, we do not report them again here. The QSO-auto, QSO×LRG, and QSO×ELG cross-correlation, and QSO fraction are the (new) measurements used to constrain the GQOD.

We use EMCEE (Foreman-Mackey et al. 2013) to sample the parameters for each of the two models in this work via a Markov chain Monte Carlo (MCMC) process. We then evaluate the autocorrelation and cross-correlation of QSOs with LRG and ELG samples using methods described in Section 3. This measurement requires pair counting to be performed at each step of sampling. We use the publicly available code CORRFUNC (Sinha 2016) to evaluate pair-counts efficiently at each iteration. We also pre-compute the overdensity field for each galaxy in the MTHOD catalogue using the method

described in Alam et al. (2019) – which is then used to evaluate the fraction of QSOs as a function of environmental overdensity. We developed a python library to efficiently create QSO samples as a function of our model parameters.[4] In this process, we use the number density of the QSO sample, treated as fixed at the mean redshift.

We use $w_p^q(r_p)$, $w_p^{qL}(r_p)$, $w_p^{qE}(r_p)$, and $f_{\rm QSO}(\delta)$ to denote the QSO autocorrelation, QSO×LRG, and QSO×ELG cross-correlation, and QSO fraction, respectively. The data and model are denoted by $\vec{D}$, $\vec{M}(\theta)$, respectively.

$$\vec{D} = \left[w_p^q(r_p),\ w_p^{qL}(r_p),\ w_p^{qE}(r_p),\ f_{\rm QSO}(\delta)\right] \tag{18}$$

$$\vec{M}(\theta) = \left[w_p^q(r_p,\theta),\ w_p^{qL}(r_p,\theta),\ w_p^{qE}(r_p,\theta),\ f_{\rm QSO}(\delta)\right]. \tag{19}$$

We then evaluate a model χ^2 using following equation:

$$\chi^2(\theta) = (\vec{D} - \vec{M}(\theta))\, C^{-1} (\vec{D} - \vec{M}(\theta))^T, \tag{20}$$

where θ represents sampling parameters and C^{-1} is the inverse covariance matrix obtained from jackknife analysis including the errors in estimate of model prediction. The MCMC process then samples the parameters according to the χ^2 given by the model.

5 RESULTS

In this section, we present our results. Our convention is to report data measurements with black data points. The two flavours of the GQOD model will be represented by red (solid) and blue (dashed) lines for the 'inherent' and 'enforced' model fits, respectively.

5.1 Clustering results

We analyse the eBOSS QSO autocorrelation and the QSO-LRG and QSO-ELG cross-correlations in redshifts of $z = 0.7$–1.1. The measurement of these statistics along with the best-fitting GQOD models is shown in Fig. 2. The top-left, top-right, and bottom-left panels of Fig. 2 show the QSO autocorrelation, $w_p^q(r_p)$, the QSO×ELG cross-correlation $w_p^{qE}(r_p)$, and the QSO×LRG cross-correlation $w_p^{qL}(r_p)$ functions, respectively. The measurement from eBOSS data is shown with black circle with error bars estimated from the jackknife sampling method. The vertical black dashed line shows the fibre collision scale at the mean redshift ($z = 0.86$) and the projected correlation function below this scale are shown with open circle and not used in the analysis. The dashed blue and solid red lines with shaded region show the enforced and inherent $f_{\rm sat}$ models, respectively, with its 1σ constraint in all panels. Note that different scales are correlated which is accounted for in our full covariance matrix.

The models describe the data very well in the range of scale considered in the current analysis. The smaller 1σ regions in the w_p^{qE} QSO×ELG correlation function is due to the higher $n_{\rm gal}$ number density of the ELG sample. Since we do not sample the smaller ('1-halo' term) scales, there is no discernible difference in the models whether or not the satellite fraction is an additional free parameter.

5.2 Environment and QSO fractions

We measure the QSO fraction as a function of galaxy overdensity environment. Recall, $f_{\rm QSO}(\delta)$ is measured straight from the data using the Voronoi cell estimation method (Section 3.3). This is presented in the bottom right panel of Fig. 2.

The QSO fraction is around 3 per cent across the whole range of environments sampled (black points in Fig. 2, bottom right). The best-fitting models (red and blue lines with 1σ shadings) again fit the data very well. The models rise monotonically from around 2.6 per cent for the least dense regions to around 3.4 per cent for the most dense environments.

In Fig. 2, we also show the LRG fraction, $f_{\rm LRG}$, as the solid (black) line and the ELG fraction (where $f_{\rm ELG} = 1 - f_{\rm LRG}$), as the dash–dotted (black) line for comparison. The behaviour of the LRG and ELG fraction with overdensity is probably dominated by galaxy quenching being more efficient in the high halo mass regime (Paper I), hence leading to the high LRG fraction in the most overdense regions. We note that the QSO fraction has essentially a flat dependence on overdensity. This is in contrast to both the LRG or ELG fractions, which have an environmental density dependence. This implies that the QSO population must contain a mixture of LRGs and ELGs as host galaxies.

5.3 Dependence on DM halo mass

Fig. 3 shows the best-fitting GQOD values derived for $f_{\rm on}$ (the fraction of galaxies that will have a QSO turned on), the fraction of QSOs that are satellites ($f_{\rm sat}$), and the number density of QSOs, $N_{\rm QSO}$, as a function of DM halo mass. As before, the best-fitting $f_{\rm sat}$ (inherent) model is given by the solid (red) line, with the $f_{\rm sat}$ (enforced) model given by the dashed (blue) line. 1σ errors are given by the shaded regions.

In the top panel of Fig. 3, we see the fraction of galaxies that have a QSO turned on is essentially independent of halo mass for both the enforced or inherent models, i.e. the probability that a galaxy has quasar activity is independent of halo mass. This is a key result: it implies that the halo mass distribution of QSOs is very broad, despite the model having freedom to choose a narrow range of halo mass through our spline fit. In order to test that the flat nature of $f_{\rm on}$ is indeed a better model we tested a lognormal model for $f_{\rm on}$. We looked at χ^2 value in a grid of mean halo mass and scatter for lognormal model finding the minimum $\chi^2/{\rm dof} = 72/53$ for a model with mean halo mas of $10^{13}\, h^{-1}{\rm M}_\odot$ with width 1.05. We also observed that the smaller width is strongly ruled out by having large value of χ^2, whereas larger width increases χ^2 marginally. When this is compared with our default model giving best fit with $\chi^2/{\rm dof} = 42/45$ then we can be more confident that the flat $f_{\rm on}$ describes the data very well.

The middle panel shows the satellite fraction as a function of halo mass. The red line shows the satellite fraction for the best-fitting inherent $f_{\rm sat}$ model, while the blue line shows the satellite fraction for the best-fitting enforced $f_{\rm sat}$ model. The fraction of satellites being QSOs rises from 0 per cent at masses above $\simeq 5 \times 10^{12}{\rm M}_\odot$. Around $\simeq 2 \times 10^{13}{\rm M}_\odot$. Both models put the fraction of QSOs being in satellites galaxies at over 50 per cent. For the dashed blue line that represents the satellite fraction in the enforced $f_{\rm sat}$, the model slightly prefers the QSOs to turn on in satellite galaxies (more notable at lower halo mass) leading the blue dashed line to always be above the red dashed line (see Section 6.2 for more discussion). Georgakakis et al. (2019) estimate the satellite fraction for AGNs as the function of X-ray luminosity finding it to be around 10–20 per cent consistent with our satellite fraction for eBOSS QSOs.

In this middle panel, we also show for comparison the fraction of satellites for LRGs and ELGs with solid black and dash–dotted lines. There are no satellite galaxies that are LRGs in haloes of $M_{\rm halo}$

[4] https://www.roe.ac.uk/~salam/GQOD/

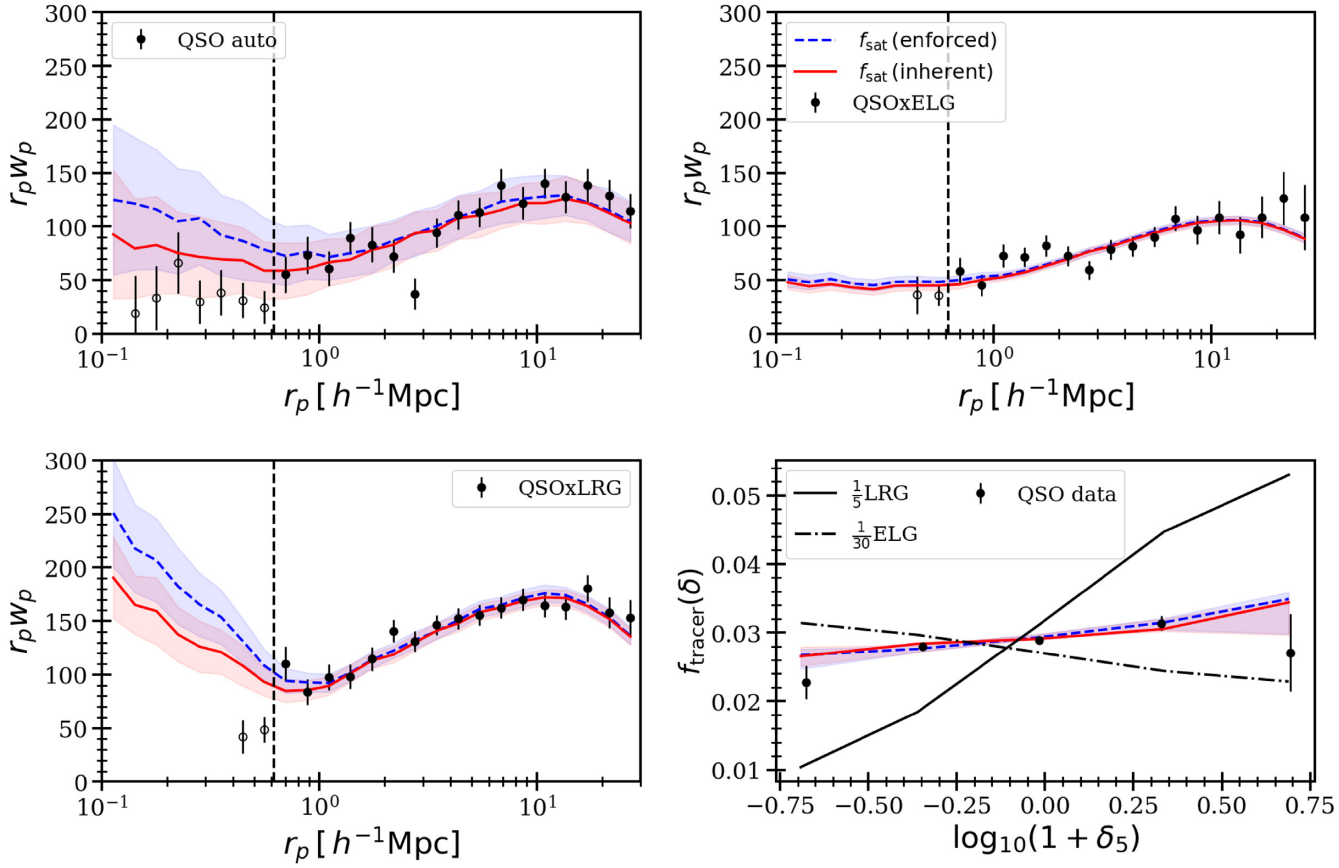

Figure 2. The top left, top right, and bottom left panels show the projected correlation function (w_p) for the QSO auto, the QSO×ELG, and QSO×LRG cross-correlation functions, respectively. The black points are the measurements from eBOSS along with the jackknife errors. The dashed vertical black line represents the fibre collision scale and data points below this are given as open circles (and not used in the analysis). The bottom right panel shows the QSO fraction as a function of environmental overdensity. For comparison, we also show the fraction of LRGs ($f_{\rm LRG}$) and ELGs ($f_{\rm ELG} = 1 - f_{\rm LRG}$) with overdensity by black solid and black dash–dotted lines, and scale by the factors given in the legend. In all panels, the blue dashed line shows the model fit with an enforced satellite fraction as additional free parameter (the shaded region giving 1σ errors). The red line shows the best-fitting model where satellite and central galaxies are equally likely to host a QSO.

$< 10^{13}\mathrm{M}_\odot$ (as found in previous LRG HOD studies: e.g. Zehavi et al. 2005; Ross et al. 2008; Reid & Spergel 2009; White et al. 2011). In haloes of $10^{13}\mathrm{M}_\odot < M_{\rm halo} < 10^{14.5}\mathrm{M}_\odot$, the fraction of satellites that are LRGs increases from 0 to just under 60 per cent. Then, for haloes with $M_{\rm halo} \gtrsim 10^{14.5}\mathrm{M}_\odot$ the fraction of satellites that are LRGs jumps to near 80 per cent. This is because a halo can only have one central but more massive haloes can have multiple objects defined as satellites (e.g. in groups and clusters); thus the satellite fraction can, and will, approach 100 per cent. The reason $f_{\rm sat}$ levels at $\simeq 60$ per cent for the LRGs is because we have many more satellites that are ELGs; in a model without ELGs, then by default the satellite fraction for LRGs would be 100 per cent in the most massive haloes.

The bottom panel shows the number density of QSOs per unit logarithmic halo mass. The black solid line shows the same distribution for the parent population scaled down by a factor of 25. We note that the halo mass distribution of QSOs is very similar to that of the host population, which comes from the fact that the turn-on probability of QSOs is independent of halo mass. We note that this predicts a very broad distribution of QSO host DM halo mass. Overall, quasars inhabit DM haloes in essentially an identical way to the full galaxy population, although they are not as common.

5.4 QSO dependence on luminosity

In Fig. 3, we also show, with the cyan line and shading, the best-fitting GQOD values derived for the enforced $f_{\rm sat}$ model, but only using the brightest 50 per cent of the QSO data.

Using the Brightest 50 per cent data, and refitting the best-fitting models, we see from Fig. 3 in the top panel that the probability for a galaxy to have quasar activity is $\simeq 50$ per cent for the brightest half of the quasar population, but remains independent of halo mass. The amplitude of the model fit simply comes from the number density; indeed, if one were to reduce the QSO population via a random sampling fraction x, then the probability of a galaxy having quasar activity will also reduce by a factor x. The key thing to note is this function remains flat, i.e. independent of halo mass.

From Fig. 3 and the cyan line in the middle panel (which is very similar to, but under the blue line/shade), the fraction of satellite galaxies that are quasars is independent of quasar luminosity.

Finally, in the bottom panel of Fig. 3, we see that overall, the 50 per cent more luminous quasars inhabit DM haloes, as function of mass, in essentially an identical way to the full QSO population. As stated above, the probability of turn on for the smaller number of more luminous QSOs is reduced, though we have same number of galaxies in our parent sample.

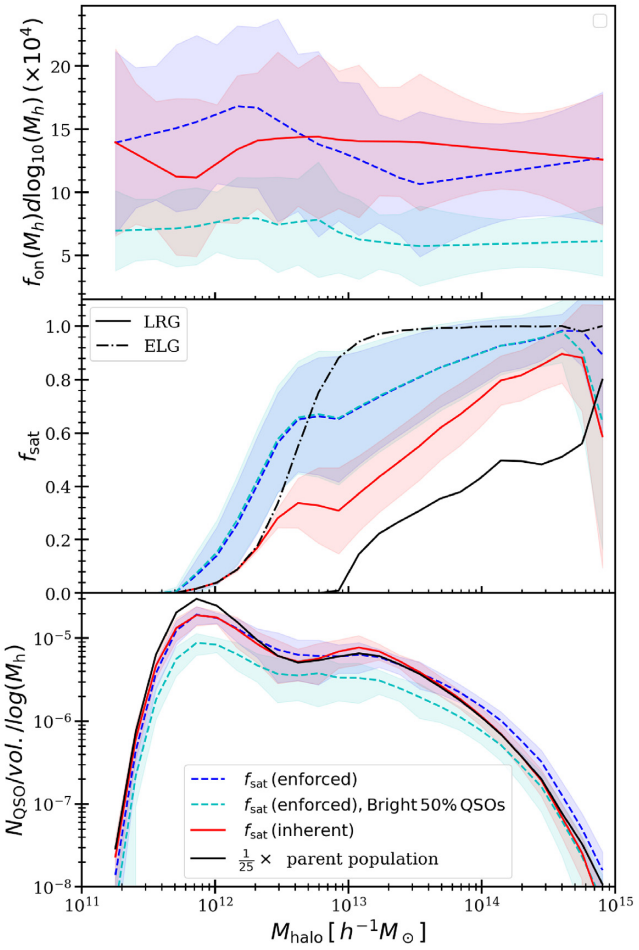

Figure 3. The top, middle, and bottom panels show f_{on}, f_{sat}, and number density of QSOs per unit logarithm of halo mass as the function of halo mass, respectively. In all panels, the dashed blue and solid red lines show the two models with enforced f_{sat} and inherent f_{sat}, respectively, with shaded regions representing 1σ errors. The f_{on} in the top panel presents the probability of a galaxy to turn on, which is also called the duty cycle of the QSO. The middle panel shows the fraction of QSOs living in satellite galaxies. For comparison, we also show in this panel the fraction of satellites for LRGs and ELGs, using black solid and dash–dotted line, respectively. The bottom panel shows number density of QSOs per unit $\log_{10}(M_h)$ and the black solid line shows the distribution for the parent galaxy population, scaled down by a factor of 25 for comparison.

5.5 QSO dependence on galaxy type and position

Fig. 4 shows the two-dimensional posterior distribution of the fraction of LRGs (f_{LRG}) and the fraction of satellites (f_{sat}) in the QSO population. The red and blue contours are the two model satellite fractions and the dark and light colour regions show 1σ and 2σ constraints.

Consider the inherent model (red contours): since the models do not contain $f_{LRG} = 1$ or $f_{LRG} = 0$, this model rules out (at the $>3\sigma$ level) the possibility that the QSO population comes entirely from either the LRG or ELG population (when we do not allow the extra degree of freedom in the inherent satellite fraction model). It also shows that roughly 20 per cent of QSO host galaxies are satellite galaxies with about 60–70 per cent of QSO hosts being an LRG galaxy.

When we allow the additional freedom from satellites in the enforced f_{sat} model (shown in blue), we are still able to rule out

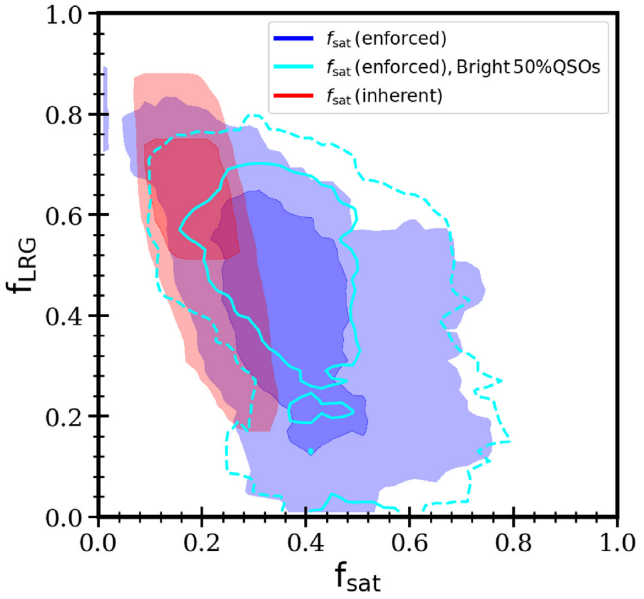

Figure 4. This shows the two-dimensional posterior of the fraction of satellites in QSOs (f_{sat}) and the fraction of LRGs in QSOs (f_{LRG}) for the two models. We note that for the red contours f_{sat} is a derived parameter, whereas for the blue contours it is a free parameter. This shows that QSOs cannot come entirely from either LRGs or ELGs but rather are a mixture with roughly equal proportions. We also note that QSOs could have significantly larger satellite fractions and in the blue contour where we allow satellites to have non-equal probabilities of converting to QSOs then we find that the data prefer even larger satellite fractions.

the possibility of the LRGs hosting the eBOSS QSO population at the 3σ level; but QSO host galaxies being entirely ELGs is possible (at the 2σ level). Allowing the additional freedom in the model, the enforced f_{sat} prefers a larger fraction, ~40 per cent, of QSO hosts to be satellite galaxies, but a lower fraction (20–60 per cent) of LRG host galaxy (compared to the inherent model). This is due to both the LRGs and satellites residing in haloes with relatively higher halo mass. Therefore, one can get the same clustering by either having a large LRG fraction with lower satellite fraction as in the inherent model, as by having a large satellite fraction with a smaller LRG fraction (as is the case for the enforced model).

It is also interesting to note that in either case the satellite fraction between 20 per cent and 40 per cent is much larger than host galaxy population and disagrees with other analysis of QSO satellite fraction (Starikova et al. 2011a; Richardson et al. 2012). Generally it is considered that large satellite fraction will mean enhanced clustering within the 1-halo term and hence our large satellite fraction might mean we overpredict the QSO autocorrelation at scales below 1 h^{-1}Mpc. But this is not the case, as shown in the top left panel of Fig. 2 where our model is consistent with the observed QSO clustering at these smaller scales. This is due to the QSO number density being very low; thus, even when we allow the model and QSOs to have a large satellite fraction, there will only be a few QSOs per halo and hence the central-satellite or satellite–satellite terms will not be as strong.

5.5.1 HSC imaging of QSO groups

Our results suggest that a large percentage of QSO host galaxies are satellites. We turn to the deep HSC imaging data to see if we can find direct examples of this.

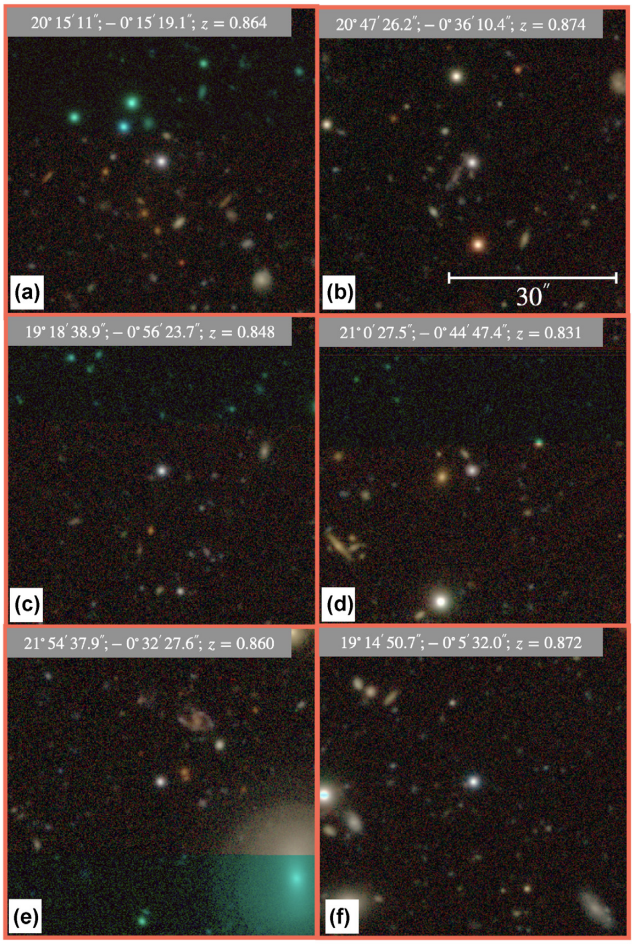

Figure 5. Cut-out images from HSC data release 2 around six different QSO randomly selected in our sample. Each of the cut-outs is centred around an eBOSS QSO, with a field of view about 1 arcmin across. This shows a sampling of the different environments that QSOs inhabit. The cut-outs were created using the HSC public data access tools.

A collage of HSC cut-outs centred on six QSOs from the eBOSS sample is shown in Fig. 5. The *RGI* filters were mapped to an RGB colour scheme using the HSC public data access tools.[5]

The six QSOs are the ones shown in the top panel of Fig. 1 with a declination cut $\delta > -1.0^{\circ}$ to restrict to the region with HSC imaging. The field of view is $\simeq$ 30 arcsec on a side, corresponding to a scale length of $\simeq 240$ kpc at $z = 0.86$ for our given cosmology.

In the collage we see several different example environments for the QSO. Note, the QSO appears in the centre of the image; this does *not* indicate at all that the QSO lies in the centre of the group, or at the peak of the DM halo. From Fig. 5, we see: in panel (a), the top left panel, the QSO in the outskirts of a red galaxy group; in panel (b), top right, the QSO in the outskirts of a blue galaxy group; in panel (c), middle left, the QSO in the centre, basically on its own; in panel (d), middle right have the QSO in a pair with an LRG; in panel (e), bottom left, the QSO is possibly in the outskirts of a galaxy group again, potentially with a massive 'Red Spiral' as the central galaxy (to the top right, '1 o'clock position' of the QSO); and finally in panel (f), bottom right, we show a QSO on its own again, but possibly the brightest object in a small group.

[5]https://hsc-gitlab.mtk.nao.ac.jp/ssp-software/data-access-tools

Without having spectroscopic redshifts for the objects in these cut-outs, it is of course very tricky to confirm galaxy group membership. However, given the depth and seeing quality of these images, and the lack of obvious foreground galaxies, it is entirely reasonable to assume we are seeing the environments of the QSOs.

6 DISCUSSION

In this section, we discuss our key results and their implications. We first discuss how the QSO population traces the underlying DM halo mass function (Section 6.1). We then place our results for the QSO satellite fraction in context, comparing with previous studies in Section 6.2. In Section 6.3, we think about the inferences that may be made from our clustering results regarding the growth history of stellar and black hole mass. In Section 6.4, we note the immediate implications of this current work and point towards future investigations.

6.1 QSOs and the DM halo mass function

One key motivation for this study was to answer the question: how do QSOs populate their DM haloes as a function of mass? Fig. 3 shows us the answer here: the parameter $f_{\rm on}$ is flat, and so the fraction of galaxies that have a QSO turned on is essentially independent of halo mass for both the enforced or inherent models. The probability that a galaxy has quasar activity is therefore independent of halo mass. The result in the bottom panel of Fig. 3 immediately follows: the QSOs sample the same DM halo mass function as the parent galaxy sample. Conroy & White (2013) find the same result. In fact, their model is consistent with QSOs being equally likely to exist in galaxies, and therefore DM haloes, over a wide range in masses and suggests a single QSO duty cycle at redshift $z < 3$.

In fact, this observation has been already recognized in the X-ray community (e.g. Leauthaud et al. 2015; Mendez et al. 2016; Powell et al. 2018; Plionis et al. 2018; Krishnan et al. 2020). All these studies find no significant differences in the clustering properties of X-ray AGNs compared to a matched galaxy sample. That is, X-ray AGNs inhabit DM haloes that are consistent on average with the overall inactive galaxy population. This result runs from the local Universe ($0.01 < z < 0.1$; Powell et al. 2018) to high redshifts, $z \simeq 4.5$ (Krishnan et al. 2020). Studying narrow-line AGNs, and comparing to a matched control samples of inactive galaxies, Li et al. (2006) find that AGNs have almost the same clustering amplitude as the control galaxies, on scales larger than a few Mpc. Here we are showing, *for the first time*, that the same is true for the blue optically selected broad-line QSOs at modest redshift.

For the Brighter 50 per cent QSO sample, we find that $f_{\rm on}$ remains flat, and thus this sample also directly maps to the same DM halo mass function as the parent galaxy sample. This is another key result as it immediately explains the lack of dependence on luminosity for QSO clustering (e.g. da Ângela et al. 2008; Shen et al. 2009, 2013; Chehade et al. 2016; Powell et al. 2020). This is consistent with the result that the QSO luminosity possibly has large scatter at fixed black hole mass and hence do not particularly correlates with the host halo mass Hickox et al. (2014).

6.2 The fraction of QSOs that are satellite galaxies

We remind the reader that our estimate of the fraction of QSOs that are in satellite galaxies comes from our GQOD model and the MTHOD mock catalogue: we derive the QSO satellite fraction, $f_{\rm sat}$, by comparing the model to the data. Our results suggest that above a

halo mass of $\simeq 10^{12}\mathrm{M}_{\odot}$ a substantial number of QSOs can be found in satellite galaxies.

A range of previous studies give a very large range of measured satellite fractions for QSOs. Richardson et al. (2012) report a satellite fraction for $z \simeq 1.4$ QSOs as $f_{\rm sat} = (7.4 \pm 1.4) \times 10^{-4}$. This is a much smaller figure than our large percentage, though it is not straightforward to compare since Richardson et al. (2012) quote a probability density function of the satellite fraction as given by all their HOD models, whereas we have the satellite fraction as a function of DM halo mass. Also, and using very similar data to Richardson et al. (2012), Kayo & Oguri (2012) find $f_{\rm sat} = 0.054^{+0.017}_{-0.016}$, i.e. nearly an order of magnitude smaller than our figure of >30 per cent at $M_{\rm halo} \gtrsim 3 \times 10^{12}\mathrm{M}_{\odot}$. This apparent discrepancy in satellite fraction can possibly be explained by realizing that these studies use small-scale pairs built from samples of binary quasars. If, for instance, binary quasars consisted of two QSOs that had very similar masses, then it is not clear that one being a satellite and the other being a central is a meaningful distinction. In this scenario, on average, a 'non-central' member of each binary quasar could be interpreted as part of a small fraction of high-mass satellites. We do note that we do not sample the 1-halo term very well (due to fiber collisions), and so suggest that our sample samples quasars in e.g. groups where the QSO can be a satellite, and this occupation fraction might be (very) different from e.g. binary QSOs in the same halo but potentially different sub-haloes.

Starikova et al. (2011b) present results showing that the Chandra/Boötes AGNs are predominantly located at the centres of DM haloes and tend to avoid satellite galaxies in haloes of this or higher mass. However, also using moderate luminosity X-ray AGNs (at $z <$ 1 from the COSMOS field), Leauthaud et al. (2015) report a mean satellite fraction of $\langle f_{\rm sat} \rangle = 18 \pm 2$ per cent.

Wang & Li (2019) is another key result here. Using a sample of 100 000 AGNs from SDSS (with the AGNs being classified via the BPT diagram, Baldwin, Phillips & Terlevich 1981, and lying mostly below $z = 0.3$), these authors also perform a clustering measurement in order to investigate the DM halo properties of narrow-line AGNs. Wang & Li (2019) investigate the central/satellite fraction for the AGNs as a function of stellar mass, and host galaxy colour, so a direct comparison to our results is tricky. However, these authors do see a substantial fraction of AGN hosts being non-central galaxies, especially at lower, $M_{\star} < 10^{10.5}\mathrm{M}_{\odot}$ stellar mass (their fig. 7).

Jiang et al. (2016) study the AGN population at low redshift and found that Type I and Type II AGNs reside in DM haloes with similar masses. But the satellite fractions of Type I AGNs are smaller than the Type II AGNs. They suggest that this has interesting implications in the QSO unified model as they detect environmental differences between Type I and Type II AGNs. It will be interesting to see in the future if a similar difference can be observed at high redshift using our model.

6.3 Host galaxy type for eBOSS QSOs

In the local Universe we observe a relationship between SMBH and host-galaxy bulge velocity dispersion (σ) and luminosity (Bell 2008; Gültekin et al. 2009; Volonteri 2010; McConnell & Ma 2013; Kormendy & Ho 2013); SMBHs are known to be related to their host bulges. Thus, it is not surprising that galaxies with generally massive bulges, such as LRGs, would be considered QSO host galaxies.

Returning to Wang & Li (2019), they find that AGNs in galaxies with blue colours at all masses, or massive red galaxies with $M_{\star} \gtrsim 10^{10.5}\mathrm{M}_{\odot}$, show almost identical clustering amplitudes at all scales to control galaxies of the same mass, colour, and structural parameters.

As mentioned above, direct comparison is difficult since our results are reported as a function of DM halo mass, and Wang & Li (2019) report stellar mass. Moreover, there is definitely not a one-to-one mapping of the red/blue galaxy population in Wang & Li (2019) to the LRG/ELG population we study. That acknowledged, we can look at broad trends. Wang & Li (2019) find that there is slight preference for AGNs to trigger in red satellite galaxies. This is broadly consistent with our findings. Wang & Li (2019) also find the blue AGNs are less likely to be satellite than the general blue galaxy population. This is again consistent with our findings (our Fig. 3, middle panel), which shows that if we allow $f_{\rm sat}$ to be a free parameter, then the QSO satellite fraction is higher at lower halo mass, but becomes less than the blue galaxies at higher halo mass. We find the transition halo mass is around $M_{\rm halo} \sim 10^{13}\mathrm{M}_{\odot}$. Wang & Li (2019) model their results with a simple halo model – where central fraction of the AGN is the only free parameter – and place AGN preferentially in the DM halo centres, but requiring a mass-dependent central fraction. Their results suggest that the mass assembly history of dark haloes may play an additional role in the AGN activity in low-mass red galaxies.

Interestingly, Krishnan et al. (2020) note that the most important property in determining the AGN clustering signal is the fraction of AGNs in passive host galaxies. This is true for our study as well using the inherent model. We note that our results are in contrast with those of Matsuoka et al. (2014), who studied high signal-to-noise spectra and inferred a very small red fraction for QSO hosts.

6.4 Quasars at intermediate redshift are not special, but they are often satellites

The results in our paper illuminate several outstanding issues in QSO physics. The mean halo mass of QSO has historically been measured to be a few $\times 10^{12}\mathrm{M}_{\odot}$, (e.g. Croom et al. 2005; Ross et al. 2009; White et al. 2012), essentially corresponding to a small group mass (cf. The Local Group having a total mass of $5.27 \times 10^{12}\mathrm{M}_{\odot}$: Li & White 2008).

Yoon et al. (2019) find that, on average, both massive quasars and massive galaxies reside in environments more than $\simeq 2$ times as dense as those of their less massive counterparts with $\log_{10}(M_{\rm BH}/M_{\odot}) < 9.0$. However, massive quasars reside in environments about $\sim$2 times less dense than inactive galaxies with $\log_{10}(M_{\rm BH}/M_{\odot}) \gtrsim 9.4$, and only about one-third of massive quasars are found in galaxy clusters, while about two-thirds of massive galaxies reside in such clusters. This indicates that massive galaxies are a much better signpost for galaxy clusters than massive quasars.

This is also what we are seeing. We are also finding QSOs to be hosted by galaxies with massive bulges, i.e. the LRGs. But the key thing is that neither the QSOs or the LRGs are necessarily central galaxies. This explains why the QSOs generally have a lower mean clustering amplitude than the massive galaxies, unless they were e.g. radio loud objects (Wake et al. 2008; Shen et al. 2009), such as the radio loud giant ellipticals (e.g. M87 or similar). Thus, a key conclusion of our work is that quasars are not special, but they may well often be satellites.

Also at $z \sim 4$, recent studies of the quasar environment find no strong evidence of luminous quasars to reside in dense environments or be associated with proto-clusters (see e.g. Uchiyama et al. 2018; also Overzier 2016 and references therein). They do find quasars to

reside in small size haloes that that are much more in accord with typical average halo masses found at lower redshifts (Eftekharzadeh et al. 2015; White et al. 2012) than reported halo mass by Shen et al. (2007).

We are also finding that QSOs can inhabit smaller haloes, of the kind that are dominated by star-forming galaxies. Possibly these two classes of object have different triggering mechanisms, but as far as optical luminosity is concerned we cannot differentiate the two cases.

7 CONCLUSIONS

In this paper, we have used the final SDSS eBOSS DR16 spectroscopic data set for LRGs, ELGs, and QSOs to make multitracer clustering measurements. The motivation is to (i) investigate how the QSO population samples the galaxy population, and (ii) to understand how the QSO host DM haloes sample the underlying DM halo distribution.

Our main conclusions are:

(i) The probability that a galaxy has quasar activity is independent of DM halo mass.

(ii) QSOs host galaxies have a large satellite fraction, probably due to their low number density (and this is possible, even without a large one-halo term).

(iii) We infer the halo mass distribution of QSOs to be very broad, independent of assumptions in modelling about the parent population.

(iv) All QSOs cannot be in LRG host galaxies (at more than the 3σ level).

(v) Likewise, all QSOs cannot correspond only to ELG host galaxies (at the $\sim 2\sigma$ level).

(vi) Given that the spline model works and that the parameter $f_{\rm on}$ is flat, the error function is generally a good model to describe $N_{\rm QSO}(M_{\rm halo})$.

The discussion of how environmental influences or assembly bias affects the QSO population is left for future studies. In the broadest sense, this self-sufficient study, in which the internally observed and measured correlation functions constrain the characteristics of the native halo catalogue, provides a much more self-consistent picture to the nuanced world of quasar occupation: (i) This likelihood-driven study grants a fair chance to multiple characteristic dependencies to arise from the measurement. The inferred indifference of the satellite fraction to the host halo mass in this picture distinguishes itself from the previous studies and reported discrepancies where the partially outsourced measurement, halo model or adapted halo mass distribution, invite a host of added assumptions and justifications. See e.g. Eftekharzadeh et al. (2019) and Kayo & Oguri (2012) for similarly adapted functional forms for the halo profile and halo mass distribution model, and yet significantly different satellite fraction that was attributed to a plausible luminosity dependency of the small-scale clustering as opposed to lack thereof on large scales. (ii) This study highlights the notion that sampling quasars that belong to a group or are otherwise members of a close-pair system (a.k.a. 'binary') leads to diverging conclusions on satellite occupation (see Section 6.2). This could be viewed as further evidence for hierarchical growth studies that have found earlier formation times for close halo pairs compared to their distant counterparts (Sheth & Tormen 1999; Harker et al. 2006).

(iii) Halo mass measurement for quasars in early eBOSS data inferred two plausible scenarios for the relatively constant characteristic halo mass between $z \sim 1$ and $z \sim 2$ (fig. 10 in Laurent et al. 2017) to be either due to massive haloes dominating the average or less luminous quasars inhabiting a wide range of halo masses and therefore putting the moderately luminous quasars in a different evolutionary path than the ∼4000 highly luminous quasars sampled by Shen et al. (2007) with a dramatically higher average halo mass. The inferred broad halo mass range in this study provides an elaborate case for the latter scenario using quasars in the same parent sample and luminosity class.

As the next generation surveys including eROSITA (Merloni et al. 2012), SKA,[6] ESA *Euclid*, the Dark Energy Spectroscopic Instrument (DESI; DESI Collaboration et al. 2016), the Prime Focus Spectrograph (PFS; Takada et al. 2014) now come online, we will be able to test our findings and fully investigate the host galaxy population of luminous AGN across cosmic history.

ACKNOWLEDGEMENTS

We thank Andy Lawrence for useful discussions. SA and JAP are supported by the European Research Council through the COSFORM Research Grant (#670193). NPR acknowledges support from the STFC and the Ernest Rutherford Fellowship scheme.

We thank Horst Meyerdierks and Eric Tittley for their support with Stacpolly and Cuillin cluster where all of the computing for this project is performed. We thank the Multi Dark Patchy Team for making their simulations publicly available. This research has made use of NASA's Astrophysics Data System. The CosmoCalculator was used (Wright 2006).

Funding for the Sloan Digital Sky Survey IV has been provided by the Alfred P. Sloan Foundation, the U.S. Department of Energy Office of Science, and the Participating Institutions. SDSS-IV acknowledges support and resources from the Center for High-Performance Computing at the University of Utah. The SDSS web site is www.sdss.org.

SDSS-IV is managed by the Astrophysical Research Consortium for the Participating Institutions of the SDSS Collaboration including the Brazilian Participation Group, the Carnegie Institution for Science, Carnegie Mellon University, the Chilean Participation Group, the French Participation Group, Harvard-Smithsonian Center for Astrophysics, Instituto de Astrofísica de Canarias, The Johns Hopkins University, Kavli Institute for the Physics and Mathematics of the Universe (IPMU) / University of Tokyo, the Korean Participation Group, Lawrence Berkeley National Laboratory, Leibniz Institut für Astrophysik Potsdam (AIP), Max-Planck-Institut für Astronomie (MPIA Heidelberg), Max-Planck-Institut für Astrophysik (MPA Garching), Max-Planck-Institut für Extraterrestrische Physik (MPE), National Astronomical Observatories of China, New Mexico State University, New York University, University of Notre Dame, Observatário Nacional / MCTI, The Ohio State University, Pennsylvania State University, Shanghai Astronomical Observatory, United Kingdom Participation Group, Universidad Nacional Autónoma de México, University of Arizona, University of Colorado Boulder, University of Oxford, University of Portsmouth, University of Utah, University of Virginia, University of Washington, University of Wisconsin, Vanderbilt University, and Yale University.

The CosmoSim data base used in this paper is a service by the Leibniz-Institute for Astrophysics Potsdam (AIP). The MultiDark data base was developed in cooperation with the Spanish MultiDark Consolider Project CSD2009-00064.

The authors gratefully acknowledge the Gauss Centre for Supercomputing e.V. (www.gauss-centre.eu) and the Partnership for Advanced Supercomputing in Europe (PRACE, www.prace-ri.eu)

[6] https://www.skatelescope.org/the-ska-project/

for funding the MultiDark simulation project by providing computing time on the GCS Supercomputer SuperMUC at Leibniz Supercomputing Centre (LRZ: www.lrz.de).

The Hyper Suprime-Cam (HSC) collaboration includes the astronomical communities of Japan and Taiwan, and Princeton University. The HSC instrumentation and software were developed by the National Astronomical Observatory of Japan (NAOJ), the Kavli Institute for the Physics and Mathematics of the Universe (Kavli IPMU), the University of Tokyo, the High Energy Accelerator Research Organization (KEK), the Academia Sinica Institute for Astronomy and Astrophysics in Taiwan (ASIAA), and Princeton University. Funding was contributed by the FIRST program from the Japanese Cabinet Office, the Ministry of Education, Culture, Sports, Science and Technology (MEXT), the Japan Society for the Promotion of Science (JSPS), Japan Science and Technology Agency (JST), the Toray Science Foundation, NAOJ, Kavli IPMU, KEK, ASIAA, and Princeton University.

This paper makes use of software developed for the Large Synoptic Survey Telescope. We thank the LSST Project for making their code available as free software at http://dm.lsst.org.

This paper is based [in part] on data collected at the Subaru Telescope and retrieved from the HSC data archive system, which is operated by Subaru Telescope and Astronomy Data Center (ADC) at National Astronomical Observatory of Japan. Data analysis was in part carried out with the cooperation of Center for Computational Astrophysics (CfCA), National Astronomical Observatory of Japan.

DATA AVAILABILITY

All of the observational data sets used in this paper are available through the SDSS website https://data.sdss.org/sas/dr16/eboss/. The codes used in this analysis along with instructions are available on https://www.roe.ac.uk/~salam/GQOD/.

REFERENCES

Aihara H. et al., 2018, PASJ, 70, S4
Aihara H. et al., 2019, PASJ, 71, 114
Alam S., Zu Y., Peacock J. A., Mand elbaum R., 2019, MNRAS, 483, 4501
Alam S., Peacock J. A., Kraljic K., Ross A. J., Comparat J., 2020, MNRAS, 497, 581
Albareti F. D. et al., 2017, ApJS, 233, 25
Anderson L. et al., 2012, MNRAS, 427, 3435
Baldwin J. A., Phillips M. M., Terlevich R., 1981, PASP, 93, 5
Bardeen J. M., Bond J. R., Kaiser N., Szalay A. S., 1986, ApJ, 304, 15
Bautista J. E. et al., 2018, ApJ, 863, 110
Behroozi P. S., Wechsler R. H., Wu H.-Y., 2013, ApJ, 762, 109
Bell E. F., 2008, ApJ, 682, 355
Berlind A. A., Weinberg D. H., 2002, ApJ, 575, 587
Bianchi D., Percival W. J., 2017, MNRAS, 472, 1106
Blanton M. R. et al., 2017, AJ, 154, 28
Bolton A. S. et al., 2012, AJ, 144, 144
Bovy J. et al., 2012, ApJ, 749, 41
Chatterjee S., Degraf C., Richardson J., Zheng Z., Nagai D., Di Matteo T., 2012, MNRAS, 419, 2657
Chehade B. et al., 2016, MNRAS, 459, 1179
Coil A. L. et al., 2004, ApJ, 609, 525
Coil A. L., Hennawi J. F., Newman J. A., Cooper M. C., Davis M., 2007, ApJ, 654, 115
Conroy C., White M., 2013, ApJ, 762, 70
Croom S. M. et al., 2005, MNRAS, 356, 415
da Ângela J. et al., 2008, MNRAS, 383, 565
Dawson K. et al., 2013, AJ, 145, 10
DESI Collaboration, 2016, preprint (arXiv:1611.00036)
Dey A. et al., 2019, AJ, 157, 168
Eftekharzadeh S. et al., 2015, MNRAS, 453, 2779
Eftekharzadeh S., Myers A. D., Kourkchi E., 2019, MNRAS, 486, 274
Fabian A. C., 2012, ARA&A, 50, 455
Foreman-Mackey D., Hogg D. W., Lang D., Goodman J., 2013, PASP, 125, 306
Georgakakis A., Comparat J., Merloni A., Ciesla L., Aird J., Finoguenov A., 2019, MNRAS, 487, 275
Gil-Marín H. et al., 2018, MNRAS, 477, 1604
Gültekin K. et al., 2009, ApJ, 698, 198
Gunn J. E. et al., 2006, AJ, 131, 2332
Guo H., Zehavi I., Zheng Z., 2012, ApJ, 756, 127
Harker G., Cole S., Helly J., Frenk C., Jenkins A., 2006, MNRAS, 367, 1039
He W. et al., 2018, PASJ, 70, S33
Hickox R. C., Mullaney J. R., Alexander D. M., Chen C.-T. J., Civano F. M., Goulding A. D., Hainline K. N., 2014, ApJ, 782, 9
Hou J. et al., 2021, MNRAS, 500, 1201
Iye M. et al., 2004, PASJ, 56, 381
Jiang N., Wang H., Mo H., Dong X.-B., Wang T., Zhou H., 2016, ApJ, 832, 111
Kayo I., Oguri M., 2012, MNRAS, 424, 1363
King A., Pounds K., 2015, ARA&A, 53, 115
Klypin A., Yepes G., Gottlöber S., Prada F., Heß S., 2016, MNRAS, 457, 4340
Kormendy J., Ho L. C., 2013, ARA&A, 51, 511
Kravtsov A. V., Berlind A. A., Wechsler R. H., Klypin A. A., Gottlöber S., Allgood B., Primack J. R., 2004, ApJ, 609, 35
Krishnan C. et al., 2020, MNRAS, 494, 1693
Krumpe M., Miyaji T., Coil A. L., Aceves H., 2012, ApJ, 746, 1
Landy S. D., Szalay A. S., 1993, ApJ, 412, 64
Laurent P. et al., 2017, J. Cosmol. Astropart. Phys., 2017, 017
Leauthaud A. et al., 2015, MNRAS, 446, 1874
Li C., Kauffmann G., Wang L., White S. D. M., Heckman T. M., Jing Y. P., 2006, MNRAS, 373, 457
Li Y.-S., White S. D. M., 2008, MNRAS, 384, 1459
Lyke B. W. et al., 2020, ApJS, 250, 8
Madau P., Dickinson M., 2014, ARA&A, 52, 415
Matsuoka Y., Strauss M. A., Price Ted N. I., DiDonato M. S., 2014, ApJ, 780, 162
McConnell N. J., Ma C.-P., 2013, ApJ, 764, 184
Mendez A. J. et al., 2016, ApJ, 821, 55
Merloni A. et al., 2012, preprint (arXiv:1209.3114)
Miyaji T., Krumpe M., Coil A. L., Aceves H., 2011, ApJ, 726, 83
Miyazaki S. et al., 2018, PASJ, 70, S1
Myers A. D. et al., 2015, ApJS, 221, 27
Myers A. D., Brunner R. J., Nichol R. C., Richards G. T., Schneider D. P., Bahcall N. A., 2007, ApJ, 658, 85
Neveux R. et al., 2020, MNRAS, 499, 210
Oogi T., Shirakata H., Nagashima M., Nishimichi T., Kawaguchi T., Okamoto T., Ishiyama T., Enoki M., 2020, MNRAS, 497, 1
Outram P. J., Shanks T., Boyle B. J., Croom S. M., Hoyle F., Loaring N. S., Miller L., Smith R. J., 2004, MNRAS, 348, 745
Overzier R. A., 2016, A&AR, 24, 14
Padovani P. et al., 2017, A&AR, 25, 2
Peebles P. J. E., 1980, The Large-Scale Structure of the Universe. Princeton University Press, Princeton
Planck Collaboration VI, 2020, A&A, 641, A6
Plionis M. et al., 2018, A&A, 620, A17
Powell M. C. et al., 2018, ApJ, 858, 110
Powell M. C., Urry C. M., Cappelluti N., Johnson J. T., LaMassa S. M., Ananna T. T., Kollmann K. E., 2020, ApJ, 891, 41
Prada F., Klypin A. A., Cuesta A. J., Betancort-Rijo J. E., Primack J., 2012, MNRAS, 423, 3018
Prakash A. et al., 2016, ApJS, 224, 34
Raichoor A. et al., 2017, MNRAS, 471, 3955
Raichoor A. et al., 2021, MNRAS, 500, 3254
Reid B. A., Spergel D. N., 2009, ApJ, 698, 143

Richardson J., Zheng Z., Chatterjee S., Nagai D., Shen Y., 2012, ApJ, 755, 30
Richardson J., Chatterjee S., Zheng Z., Myers A. D., Hickox R., 2013, ApJ, 774, 143
Rodríguez-Torres S. A. et al., 2017, MNRAS, 468, 728
Ross N. P. et al., 2009, ApJ, 697, 1634
Ross A. J. et al., 2012, MNRAS, 424, 564
Ross A. et al., 2020, MNRAS, 498, 2354
Ross N. P., Shanks T., Cannon R. D., Wake D. A., Sharp R. G., Croom S. M., Peacock J. A., 2008, MNRAS, 387, 1323
Shen Y. et al., 2007, AJ, 133, 2222
Shen Y. et al., 2009, ApJ, 697, 1656
Shen Y. et al., 2013, ApJ, 778, 98
Sheth R. K., Tormen G., 1999, MNRAS, 308, 119
Sinha M., 2016, Corrfunc: Corrfunc-1.1.0
Smee S. A. et al., 2013, AJ, 146, 32
Somerville R. S., Davé R., 2015, ARA&A, 53, 51
Starikova S. et al., 2011a, ApJ, 741, 15
Starikova S. et al., 2011b, ApJ, 741, 15
Takada M. et al., 2014, PASJ, 66, R1
Uchiyama H. et al., 2018, PASJ, 70, S32
Umetsu K. et al., 2020, ApJ, 890, 148
Volonteri M., 2010, A&AR, 18, 279
Wake D. A., Croom S. M., Sadler E. M., Johnston H. M., 2008, MNRAS, 391, 1674
Wang L., Li C., 2019, MNRAS, 483, 1452
Wang L., Weinmann S. M., De Lucia G., Yang X., 2013, MNRAS, 433, 515
White M. et al., 2011, ApJ, 728, 126
White M. et al., 2012, MNRAS, 999, 126
Wright E. L. et al., 2010, AJ, 140, 1868
Wright E. L., 2006, PASP, 118, 1711
Xue Y. Q., 2017, New Astron. Rev., 79, 59
Yoon Y., Im M., Hyun M., Jun H. D., Hwang N., Kim M., Park B.-G., 2019, ApJ, 871, 57
Zehavi I. et al., 2005, ApJ, 630, 1
Zheng Z. et al., 2005, ApJ, 633, 791
Zheng Z., Zehavi I., Eisenstein D. J., Weinberg D. H., Jing Y. P., 2009, ApJ, 707, 554

APPENDIX: QSO 50 PER CENT BRIGHT SAMPLE

Fig. A1 shows a version of data and the best-fitting model including QSO Bright sample.

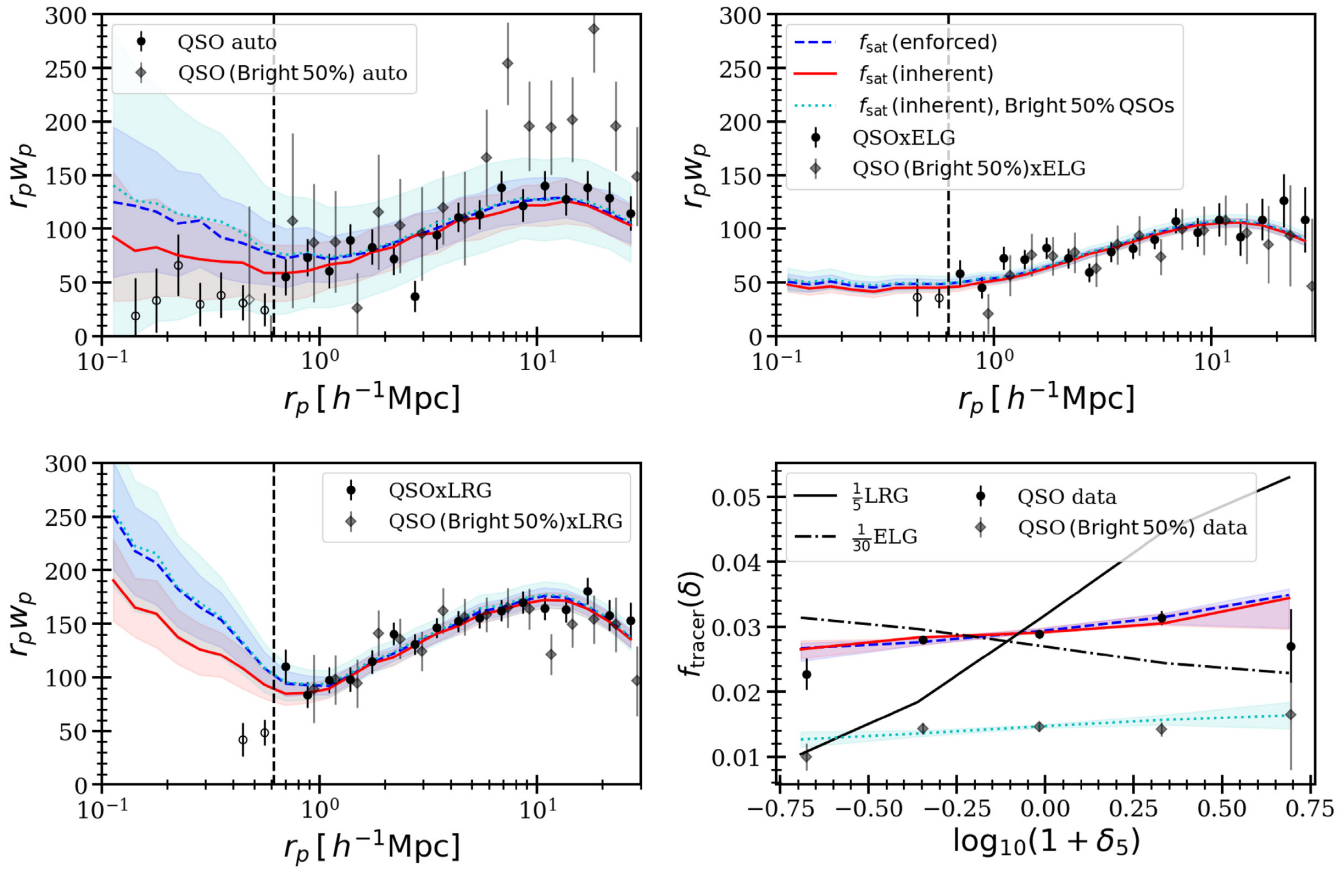

Figure A1. Same as Fig. 2 but including QSO Bright 50 per cent sample. The diamond points in each panel shows the measurements from the Bright QSO sample, whereas the dotted cyan line with shaded region shows the best-fitting model to QSO Bright sample along with 1σ spread.

This paper has been typeset from a TEX/LATEX file prepared by the author.

List of astronomical key words (Updated on 2020 January)

This list is common to *Monthly Notices of the Royal Astronomical Society, Astronomy and Astrophysics*, and *The Astrophysical Journal*. In order to ease the search, the key words are subdivided into broad categories. No more than *six* subcategories altogether should be listed for a paper.

The subcategories in boldface containing the word 'individual' are intended for use with specific astronomical objects; these should never be used alone, but always in combination with the most common names for the astronomical objects in question. Note that each object counts as one subcategory within the allowed limit of six.

The parts of the key words in italics are for reference only and should be omitted when the keywords are entered on the manuscript.

General
editorials, notices
errata, addenda
extraterrestrial intelligence
history and philosophy of astronomy
miscellaneous
obituaries, biographies
publications, bibliography
sociology of astronomy
standards

Physical data and processes
acceleration of particles
accretion, accretion discs
asteroseismology
astrobiology
astrochemistry
astroparticle physics
atomic data
atomic processes
black hole physics
chaos
conduction
convection
dense matter
diffusion
dynamo
elementary particles
equation of state
gravitation
gravitational lensing: micro
gravitational lensing: strong
gravitational lensing: weak
gravitational waves
hydrodynamics
instabilities
line: formation
line: identification
line: profiles
magnetic fields
magnetic reconnection
(magnetohydrodynamics) MHD
masers
molecular data
molecular processes
neutrinos
nuclear reactions, nucleosynthesis, abundances
opacity
plasmas
polarization
radiation: dynamics
radiation mechanisms:general
radiation mechanisms: non-thermal
radiation mechanisms: thermal
radiative transfer
relativistic processes
scattering
shock waves
solid state: refractory
solid state: volatile
turbulence
waves

Astronomical instrumentation, methods and techniques
atmospheric effects
balloons
instrumentation: adaptive optics
instrumentation: detectors
instrumentation: high angular resolution
instrumentation: interferometers
instrumentation: miscellaneous
instrumentation: photometers
instrumentation: polarimeters
instrumentation: spectrographs
light pollution
methods: analytical
methods: data analysis
methods: laboratory: atomic
methods: laboratory: molecular
methods: laboratory: solid state
methods: miscellaneous
methods: numerical
methods: observational
methods: statistical
site testing
space vehicles
space vehicles: instruments
techniques: high angular resolution
techniques: image processing
techniques: imaging spectroscopy
techniques: interferometric
techniques: miscellaneous
techniques: photometric
techniques: polarimetric
techniques: radar astronomy
techniques: radial velocities
techniques: spectroscopic
telescopes

Astronomical data bases
astronomical data bases: miscellaneous
atlases
catalogues
surveys
virtual observatory tools

Software
software: data analysis
software: development
software: documentation
software: public release
software: simulations

Astrometry and celestial mechanics
astrometry
celestial mechanics
eclipses
ephemerides
occultations
parallaxes
proper motions
reference systems
time

The Sun
Sun: abundances
Sun: activity
Sun: atmosphere
Sun: chromosphere
Sun: corona
Sun: coronal mass ejections (CMEs)
Sun: evolution
Sun: faculae, plages
Sun: filaments, prominences
Sun: flares
Sun: fundamental parameters
Sun: general
Sun: granulation
Sun: helioseismology
Sun: heliosphere
Sun: infrared
Sun: interior
Sun: magnetic fields
Sun: oscillations
Sun: particle emission
Sun: photosphere
Sun: radio radiation
Sun: rotation
(Sun:) solar–terrestrial relations
(Sun:) solar wind
(Sun:) sunspots
Sun: transition region
Sun: UV radiation
Sun: X-rays, gamma-rays

Planetary systems
comets: general

comets: individual: . . .
Earth
interplanetary medium
Kuiper belt: general

Kuiper belt objects: individual: . . .
meteorites, meteors, meteoroids
minor planets, asteroids: general

minor planets, asteroids: individual: . . .
Moon
Oort Cloud
planets and satellites: atmospheres
planets and satellites: aurorae
planets and satellites: composition
planets and satellites: detection
planets and satellites: dynamical evolution and stability
planets and satellites: formation
planets and satellites: fundamental parameters
planets and satellites: gaseous planets
planets and satellites: general

planets and satellites: individual: . . .
planets and satellites: interiors
planets and satellites: magnetic fields
planets and satellites: oceans
planets and satellites: physical evolution
planets and satellites: rings
planets and satellites: surfaces
planets and satellites: tectonics
planets and satellites: terrestrial planets
planet–disc interactions
planet–star interactions
protoplanetary discs
zodiacal dust

Stars
stars: abundances
stars: activity
stars: AGB and post-AGB
stars: atmospheres
(stars:) binaries *(including multiple)*: close
(stars:) binaries: eclipsing
(stars:) binaries: general
(stars:) binaries: spectroscopic
(stars:) binaries: symbiotic
(stars:) binaries: visual
stars: black holes
(stars:) blue stragglers
(stars:) brown dwarfs
stars: carbon
stars: chemically peculiar
stars: chromospheres
(stars:) circumstellar matter
stars: coronae
stars: distances
stars: dwarf novae
stars: early-type
stars: emission-line, Be
stars: evolution
stars: flare
stars: formation
stars: fundamental parameters
(stars:) gamma-ray burst: general
(stars:) **gamma-ray burst: individual: . . .**
stars: general
(stars:) Hertzsprung–Russell and colour–magnitude diagrams
stars: horizontal branch
stars: imaging
stars: individual: . . .
stars: interiors

stars: jets
stars: kinematics and dynamics
stars: late-type
stars: low-mass
stars: luminosity function, mass function
stars: magnetars
stars: magnetic field
stars: massive
stars: mass-loss
stars: neutron
(stars:) novae, cataclysmic variables
stars: oscillations *(including pulsations)*
stars: peculiar *(except chemically peculiar)*
(stars:) planetary systems
stars: Population II
stars: Population III
stars: pre-main-sequence
stars: protostars
(stars:) pulsars: general
(stars:) **pulsars: individual: . . .**
stars: rotation
stars: solar-type
(stars:) starspots
stars: statistics
(stars:) subdwarfs
(stars:) supergiants
(stars:) supernovae: general
(stars:) **supernovae: individual: . . .**
stars: variables: Cepheids
stars: variables: Scuti
stars: variables: general
stars: variables: RR Lyrae
stars: variables: S Doradus
stars: variables: T Tauri, Herbig Ae/Be
(stars:) white dwarfs
stars: winds, outflows
stars: Wolf–Rayet

Interstellar medium (ISM), nebulae
ISM: abundances
ISM: atoms
ISM: bubbles
ISM: clouds
(ISM:) cosmic rays
(ISM:) dust, extinction
ISM: evolution
ISM: general
(ISM:) HII regions
(ISM:) Herbig–Haro objects

ISM: individual objects: . . .
(except planetary nebulae)
ISM: jets and outflows
ISM: kinematics and dynamics
ISM: lines and bands
ISM: magnetic fields
ISM: molecules
(ISM:) photodissociation region (PDR)
(ISM:) planetary nebulae: general
(ISM:) **planetary nebulae: individual: . . .**
ISM: structure
ISM: supernova remnants

The Galaxy
Galaxy: abundances
Galaxy: bulge
Galaxy: centre
Galaxy: disc
Galaxy: evolution
Galaxy: formation
Galaxy: fundamental parameters
Galaxy: general
(Galaxy:) globular clusters: general
(Galaxy:) **globular clusters: individual: . . .**
Galaxy: halo
Galaxy: kinematics and dynamics
(Galaxy:) local interstellar matter
Galaxy: nucleus
(Galaxy:) open clusters and associations: general
(Galaxy:) **open clusters and associations: individual: . . .**
(Galaxy:) solar neighbourhood
Galaxy: stellar content
Galaxy: structure

Galaxies
galaxies: abundances
galaxies: active
galaxies: bar
(galaxies:) BL Lacertae objects: general
(galaxies:) **BL Lacertae objects: individual: . . .**
galaxies: bulges
galaxies: clusters: general

galaxies: clusters: individual: . . .
galaxies: clusters: intracluster medium
galaxies: disc
galaxies: distances and redshifts
galaxies: dwarf
galaxies: elliptical and lenticular, cD
galaxies: evolution
galaxies: formation
galaxies: fundamental parameters
galaxies: general
galaxies: groups: general

galaxies: groups: individual: . . .
galaxies: haloes
galaxies: high-redshift

galaxies: individual: . . .
galaxies: interactions
(galaxies:) intergalactic medium
galaxies: irregular
galaxies: ISM
galaxies: jets
galaxies: kinematics and dynamics
(galaxies:) Local Group
galaxies: luminosity function, mass function
(galaxies:) Magellanic Clouds
galaxies: magnetic fields
galaxies: nuclei
galaxies: peculiar
galaxies: photometry
(galaxies:) quasars: absorption lines
(galaxies:) quasars: emission lines
(galaxies:) quasars: general

(galaxies:) **quasars: individual: . . .**
(galaxies:) quasars: supermassive black holes
galaxies: Seyfert
galaxies: spiral
galaxies: starburst
galaxies: star clusters: general

galaxies: star clusters: individual: . . .
galaxies: star formation
galaxies: statistics
galaxies: stellar content
galaxies: structure

Cosmology
(cosmology:) cosmic background radiation
(cosmology:) cosmological parameters
(cosmology:) dark ages, reionization, first stars
(cosmology:) dark energy
(cosmology:) dark matter
(cosmology:) diffuse radiation
(cosmology:) distance scale
(cosmology:) early Universe
(cosmology:) inflation
(cosmology:) large-scale structure of Universe
cosmology: miscellaneous
cosmology: observations
(cosmology:) primordial nucleosynthesis
cosmology: theory

Resolved and unresolved sources as a function of wavelength
gamma-rays: diffuse background
gamma-rays: galaxies
gamma-rays: galaxies: clusters
gamma-rays: general
gamma-rays: ISM
gamma-rays: stars
infrared: diffuse background
infrared: galaxies
infrared: general
infrared: ISM
infrared: planetary systems
infrared: stars
radio continuum: galaxies
radio continuum: general
radio continuum: ISM
radio continuum: planetary systems
radio continuum: stars
radio continuum: transients
radio lines: galaxies
radio lines: general
radio lines: ISM
radio lines: planetary systems
radio lines: stars
submillimetre: diffuse background
submillimetre: galaxies
submillimetre: general
submillimetre: ISM
submillimetre: planetary systems
submillimetre: stars
ultraviolet: galaxies
ultraviolet: general
ultraviolet: ISM
ultraviolet: planetary systems
ultraviolet: stars
X-rays: binaries
X-rays: bursts
X-rays: diffuse background
X-rays: galaxies
X-rays: galaxies: clusters
X-rays: general
X-rays: individual: . . .
X-rays: ISM
X-rays: stars

Transients
(transients:) black hole mergers
(transients:) black hole - neutron star mergers
(transients:) fast radio bursts
(transients:) gamma-ray bursts
(transients:) neutron star mergers
transients: novae
transients: supernovae
transients: tidal disruption events